

---

This manuscript is a preprint and has not undergone peer-review. Please note that subsequent versions of this manuscript may have different content. If accepted, the final version of this manuscript will be available via the 'Peer-reviewed Publication DOI' link on the right-hand side of this webpage. Please feel free to contact any of the authors, we welcome feedback!

---

1 Transformation of dense shelf water cascade into turbidity  
2 currents: insights from high-resolution geophysical datasets

3 Nan Wu<sup>1\*</sup>, Guangfa Zhong<sup>1</sup>, Yakufu Niyazi<sup>2</sup>, Biwen Wang<sup>1</sup>, Harya D. Nugraha<sup>3</sup>,

4 Michael J. Steventon<sup>4</sup>

5 <sup>1</sup>State Key Laboratory of Marine Geology, Tongji University, 1239 Siping Road,  
6 Shanghai, 200092, China

7 <sup>2</sup>Minderoo-UWA Deep-Sea Research Centre, School of Biological Sciences and UWA  
8 Oceans Institute, The University of Western Australia, Perth, WA 6009, Australia

9 <sup>3</sup>Center for Sustainable Geoscience, Universitas Pertamina, Jakarta, 12220, Indonesia

10 <sup>4</sup>Shell Research, Shell Centre, London, SE1 7NA, UK

11 \*Email: [nanwu@tongji.edu.cn](mailto:nanwu@tongji.edu.cn)

12  
13 **ABSTRACT**

14 Dense shelf water cascade (DSWC) is a common oceanographic phenomenon on many  
15 continental shelves. Previous studies indicate that the DSWC could shape seabed  
16 physiography and carry seawater, sediment, and organic carbon a long distance from  
17 the continental shelf to the basin floor. However, it remains enigmatic how these  
18 DSWC's interact with seabed geomorphology and travel long distances from the  
19 shallow to deep marine environments. In this study, we employed high-resolution  
20 multibeam bathymetry, 2D and 3D seismic reflection, core description, and sediment  
21 grain size data from the Gippsland Basin, southeast offshore Australia. The continental  
22 shelf of the central Gippsland Basin stores sediment supplied by the along-shelf

23 transported DSWC. By calculating the sediment motion threshold, we demonstrate  
24 that the DSWC is capable of entraining sediment from, and forming dense bottom  
25 nepheloid layers above, the seabed. Seismic reflection data reveal that cyclic steps are  
26 common on the shelf and slope, indicating a downslope-transported, supercritical  
27 current-dominated environment. Core observation and grain size analyses reveal that  
28 coarse-grained, Ta-typed turbidites are the major facies, indicating the presence of  
29 high-intensity downslope-traversing turbidity currents. Thus, supercritical turbidity  
30 currents are the dominant sedimentary process in the central Gippsland Basin. We  
31 illuminate that DSWC can interact with pre-existing seabed bathymetry created by a  
32 buried submarine landslide, resuspending sediment and igniting downslope-  
33 transported turbidity currents. The presence of numerous cyclic steps indicates that  
34 the turbidity current can evolve into a supercritical regime upon ignition, leaving  
35 complex seabed geomorphology and allowing the forming currents to travel across the  
36 shelf and extend more than 80 km down the lower slope. As revealed by our literature  
37 review, we imply that the transformation of DSWC into turbidity currents should be a  
38 common sedimentary process on outer continental shelves globally, significantly  
39 sculpting the seabed morphology and facilitating sediment and other marine particles  
40 transportation from shallow to deep sea.

41 Keywords: Dense shelf water cascade (DSWC), Current transformation, Turbidity-  
42 current initiation, Gippsland Basin

43

## 44 1. INTRODUCTION

45 Along the continental shelves, seasonal evaporation during summer and cooling  
46 during winter can generate a cross-shelf density gradient that drives denser seawater  
47 transport seawards along the seabed (Ivanov et al., 2004; Canals et al., 2006). This  
48 process is defined as a dense shelf water cascade (hereafter DSWC). The DSWC is a  
49 climate-driven oceanographic phenomenon prominent throughout the tropical to the  
50 high-latitude continental margins (Figure 1A; Ivanov et al., 2004; Amblas and  
51 Dowdeswell, 2018; Mahjabin et al., 2020; Gales et al., 2021). The DSWC has been  
52 repeatedly measured and well-studied by both long-term and high-frequency in situ  
53 measurements in physical oceanography observations (i.e. Canals et al., 2006; Puig et  
54 al., 2008; Canals et al., 2009). Once the DSWC is initiated, it sinks and overflows the  
55 outer shelf area under the influence of gravity, cascading downslope until it reaches  
56 its density equilibrium depth (also known as neutral density level; Figure 1B)  
57 (Fohrmann et al., 1998; Canals et al., 2009). Results indicate the DSWC can travel more  
58 than 10,000 km along the coastline and descends more than 1000 m down the slope  
59 and eventually flooding the basin floor (Figure 1B; Ivanov et al., 2004; Canals et al.,  
60 2009; Mahjabin et al., 2020). When transported along the shelf, DSWC can travel at a  
61 high speed (i.e. 1.2 m/s) and is highly erosive (Canals et al., 2006; Puig, 2017). For  
62 example, the DSWC can dislodge a c. 400 kg anchor at least 3 km away from its mooring  
63 position, and polish the rusty iron of the train wheel very shiny through continuous  
64 sandblasting associated with the powerful cascading currents (Puig et al., 2008).

65

66 The DSWC can affect a large portion of the seabed, induce erosion and deposition, and

67 generate bottom nepheloid layers (zones) that contain significant amounts of  
68 suspended sediments and subsequently produce fast travelling gravity flows (Figure  
69 1B; Canals et al., 2006; Puig, 2017). At specific locations, canyons are often the major  
70 conduits and determine the paths and spreading conditions for the DSWC (Canals et  
71 al., 2006; Morrison et al., 2020; Gales et al., 2021). The DSWC has proved to be an  
72 effective seabed-sculpting agent and is capable of transferring large amounts of water  
73 and heat, sediments, organic carbon, marine pollutants and nutrients from the shallow  
74 marine to the deep ocean (Canals et al., 2006; Puig et al., 2008; Canals et al., 2009).  
75 Therefore, the DSWC plays an important role in global deep-ocean circulation,  
76 sediment source-to-sink, earth's climate system, and carbon and biogeochemical  
77 cycles (Amblas and Dowdeswell, 2018).

78

79 Despite the extensive existing literature, some important questions remain to be  
80 addressed. Firstly, the process of how DSWC produces gravity flows and shape seabed  
81 geomorphology is still poorly understood (Canals et al., 2006; Talling, 2014). Secondly,  
82 the reasons for the DSWC spreading over a considerable distance across the shelf and  
83 even reaching the lower slope remain unclear. Here we attempt to unravel these  
84 important, yet under-explored aspects of DSWC, by presenting observations based on  
85 high-resolution bathymetric multibeam, seismic reflection, piston core and sediment  
86 grain size datasets from the offshore Gippsland Basin, Australia. The occurrence of the  
87 DSWC has brought a large amount of sediment and resulted in extremely complex  
88 seabed geomorphology in the central Gippsland Basin (Godfrey et al., 1980; Tomczak,

89 1985; Mitchell et al., 2007b). The complex seabed geomorphology reflects the action  
90 of a range of oceanographic and sedimentary processes at multiple spatiotemporal  
91 scales. Therefore, the central region of the Gippsland Basin provides an ideal place to  
92 investigate the remaining questions we raised above. We revealed that the DSWC can  
93 interact with pre-existing seabed depressions caused by deposited submarine  
94 landslide, igniting turbidity currents and leaving erosional bedforms on the seabed.  
95 We highlight that the transformation of the DSWC into turbidity currents is an  
96 underappreciated sedimentary process that should be common on outer continental  
97 shelves globally. The transition from the DSWC to the turbidity current is crucial to  
98 understanding the evolution of seabed geomorphology through time, as well as the  
99 mechanisms that account for the long-distance transportation of the DSWC under the  
100 influence of dynamic oceanographic processes.

101

## 102 2. GEOLOGICAL SETTING

### 103 2.1 The Gippsland Basin

104 The offshore Gippsland Basin is dominated by a cool-water carbonate system located  
105 on SE Australia's passive margin, between the mainland of Australia and Tasmania  
106 (Figures 2A, 2B; Rahmanian et al., 1990). It is one of Australia's most prolific  
107 hydrocarbon provinces, fisheries, and potential carbon storage, and holds a number of  
108 other potential marine resource applications (Rahmanian et al., 1990; Mitchell et al.,  
109 2007a; Mitchell et al., 2007b). The Gippsland Basin belongs to a series of rift basins  
110 formed along the southern margin of the Australian plate, due to the separation of

111 Antarctica and Australian continents during the breakup of Gondwana in the Mesozoic  
112 (Colwell et al., 1993). Since the Pleistocene, the Gippsland Basin has been detached  
113 from major river sources, allowing the development of a cool water carbonate  
114 province with minimal terrigenous input (Mitchell et al., 2007b). The margin of the  
115 Gippsland Basin is dominated by a c. 100 km wide embayment, and the SE margin of  
116 the basin is floored by c. 120 km long and 15-70 km wide, ESE-trending Bass Canyon  
117 system (Figures 2A, 2B). The Bass Canyon is one of the world's largest submarine  
118 canyons and constitutes the SE boundary of the Gippsland Basin (Mitchell et al.,  
119 2007b). The Bass Canyon has acted as a major conduit and key element in the source-  
120 to-sink system in the SE Australian area since the Late Cretaceous (approximately  
121 80Ma; Hill et al., 1998). At present, it still transfers sediments, oxygen, nutrients,  
122 pollutants, and organic matter from the canyon head to the Tasman Abyssal Plain at  
123 almost 4500 m water depth (Figure 2B).

124

## 125 2.2 Climate and oceanography

126 The Bass Strait is a shallow (water depth range from 40-60 m) coastal sea between  
127 mainland Australia and Tasmania, connecting the Great Australian Bight in the west  
128 and the Tasman Sea in the east (Figure 2A; Tomczak, 1985; Lavering, 1994). In winter,  
129 the shallow Bass Strait imposes a limit on the penetration of thermal convection, and  
130 as a consequence, Bass Strait seawater cools rapidly and has a higher salinity than that  
131 of the surface layer in the Tasman Sea (Lavering, 1994). Therefore, when seawater  
132 leaves the Bass Strait on its eastern side, it has a prominent density contrast against

133 the Tasman Sea water (Tomczak, 1985). As a consequence, cold, denser Bass Strait  
134 seawater can flow into and sink beneath the warmer, fresher water of the Gippsland  
135 shelf, generating the northeast-flowing Bass Cascade Current (hereafter BCC) which  
136 sinks to the 200-400 m isobaths and extends more than tens of kilometres (Figure 2B;  
137 Godfrey et al., 1980; Li et al., 2005; Mitchell et al., 2007b). Observations from the  
138 ocean bottom stations have revealed that the BCC is the densest seawater offshore SE  
139 Australia, it is active every year and is with an average transport rate of 1.0 Sverdrups  
140 (Sv;  $1\text{Sv}=10^6 \text{ m}^3/\text{s}$ ) (Middleton and Bye, 2007). The transportation of BCC has  
141 transported significant quantities of water and sediments and spread along the shelf  
142 edge over a long distance (Boland, 1971). For example, distinctive temperature-salinity  
143 anomalies are found at 200-800 m depth in the Tasman Sea, most likely caused by Bass  
144 Strait seawater penetration (Figure 2C; Boland, 1971). In the Gippsland Basin, the  
145 central continental shelf is dominated by the Westerly wind throughout the year  
146 (especially in winter; Figure 2B; Li et al., 2005). The eastward-flowing Westerly wind  
147 flows at 10-30 km/h with maximum gusts reaching 100 km/h. Therefore, the Westerly  
148 wind has created a moderate to high energy wave-dominated environment and a  
149 robust NE-transported Ekman Transport Flow (ETF) in a water depth of c. 200-300 m  
150 (Figure 2B; Mitchell et al., 2007a; O'Brien et al., 2018). The East Australia Current (EAC)  
151 is a western boundary current that carries warm equatorial waters and flows  
152 southward adjacent to Australia's southeast coast (Figure 2B, 2D). It is up to 500 m  
153 deep and 100 km wide, occasionally extending far enough south to reverse the  
154 movement of water in the Gippsland Basin during summer months (Li et al., 2005).



155 Therefore, the combination of seasonal northward flowing BCC, the southward flowing  
156 EAC, and northeast flowing ETF have jointly controlled the oceanography and  
157 sedimentation along SE Australia's continental margin.

158

### 159 3. DATASET AND METHODOLOGY

160 The datasets available for this study include multibeam bathymetry data with a  
161 coverage area of c. 250,000 km<sup>2</sup>, 2D and 3D seismic reflection data with a coverage  
162 area of c. 1700 km<sup>2</sup>, with lithology control provided by six-piston core samples (Figures  
163 2B, 3A).

164

#### 165 3.1 Multibeam bathymetry

166 Multibeam bathymetry data for this study is sourced and can be downloaded from  
167 Geoscience Australia's Marine data portal (<http://marine.ga.gov.au>). The dataset is  
168 compiled from multiple bathymetric surveys and gridded at 50x50 m; hence,  
169 geomorphological features smaller than 50 m across cannot be differentiated. The  
170 multibeam bathymetry dataset covers the Gippsland Basin continental shelf, at around  
171 200 m water depth, to the Tasman Sea Abyssal plain, at over 4000 m water depth  
172 (Figure 3A).

173

#### 174 3.2 Seismic data

175 We adopt two types of seismic reflection data provided by Geoscience Australia  
176 (<http://www.ga.gov.au/nopims>): (i) A 2D regional seismic section which is up to c. 90

177 km long, therefore providing excellent coverage from Gippsland Basin shelf region to  
178 Bass Canyon abyssal plain (Figure 3C); and (ii) two 3D seismic reflection surveys (Elver  
179 3D and Tuskfish 3D), which covered an area of c. 650 km<sup>2</sup> and 1050 km<sup>2</sup>, respectively  
180 (Figure 2B). Both 3D seismic datasets are post-stack time-migrated and zero-phase  
181 processed, and a downward decrease and increase in acoustic impedance are  
182 expressed as blue (negative) and red (positive) seismic reflections, respectively. The  
183 3D seismic surveys have a dominant frequency content of 70 hertz and an average  
184 seismic velocity of 1700 m/s near the seabed sediment, which gives an approximate  
185 vertical resolution of c. 6 m for the near seabed sediments. The 3D seismic resolution  
186 is therefore sufficient to map the geometry of detailed seabed sedimentary and  
187 structural features. We further extract the dip illumination seismic attribute (see  
188 Appendix S1 for an explanation), from the 3D seismic dataset to determine the seabed  
189 geometries and geomorphology of the interpreted submarine deposits.

190

### 191 3.3 Piston Core and grain Size

192 Comprehensive sediment sampling and piston cores collection was conducted from  
193 RV Franklin cruise in 1998 (FR11/98) (Exon et al., 2002). In this study, we adopted six-  
194 piston cores in the continental shelf and slope areas over a water depth range of 200-  
195 2500 m. The detailed core descriptions and interpretations are compiled from  
196 (Mitchell et al., 2007b), which have provided lithological and sedimentary facies  
197 constraints for the study area. In addition, we analyzed seabed grain size distribution  
198 data from 13 locations, obtained from the Geoscience Australia Marine Sediment

199 Database (<https://portal.ga.gov.au>). For the purpose of this current research, we  
200 analyzed the proportion of mud (<65  $\mu\text{m}$ ), sand (between 65  $\mu\text{m}$  and 2 mm) and gravel  
201 (> 2mm) within each sampling locations.

202

### 203 3.4 Sediment incipient motion calculation

204 To determine whether BCC can entrain and suspend sediments during transportation,  
205 we calculate the critical condition for sediment incipient motion using the method  
206 proposed by Soulsby (1997). Soulsby (1997) equations resolve critical seabed shear  
207 stress ( $\tau_{cr}$ ) and bottom shear stress due to currents ( $\tau_b$ ), if  $\tau_b < \tau_{cr}$ , the seabed  
208 sediments are immobile (i.e. no movement), if  $\tau_b > \tau_{cr}$ , the seabed sediments move  
209 and could be suspended and transported (Soulsby, 1997). In continental shelf settings,  
210 Soulsby (1997) method is widely applied and has been proved effective for quantifying  
211 the threshold of sediment motion under marine current environments (i.e. Villacieros-  
212 Robineau et al., 2019).

213

214 The  $\tau_{cr}$  of seabed composed mainly of cohesive sediments was calculated using  
215 Equations (1) - (3) from Soulsby (1997).

$$216 \quad \tau_{cr} = g\theta_{cr}(\rho_s - \rho_w)d \quad (1)$$

$$217 \quad \theta_{cr} = 0.3 / (1 + 1.2D_*) + 0.055(1 - e^{-0.02D_*}) \quad (2)$$

$$218 \quad D_* = [g(\rho_s - \rho_w) / (\rho_w v^2)]^{1/3}d \quad (3)$$

219 where  $g$  is gravitational acceleration, 9.81  $\text{m/s}^2$ ;  $\rho_s$  is sediment density, 2,650  
220  $\text{kg/m}^3$ ;  $\rho_w$  is current density of BCC, 1,023.2  $\text{kg/m}^3$  according to Tomczak (1987);  $d$

221 is sediment grain size, ranging from 65  $\mu\text{m}$  to 2 mm on the continental shelf of  
222 Gippsland Basin (Figure 8D);  $\theta_{cr}$  is critical Shields parameter;  $D_*$  is dimensionless  
223 grain size parameter;  $\nu$  is kinematic viscosity for seawater,  $1.212 \times 10^{-6} \text{ m}^2/\text{s}$  at 35  
224 salinity and 15  $^\circ\text{C}$  (Luick et al., 1994).

225

226 The bottom shear stress  $\tau_b$  and the shear velocity  $u^*$  impacted by currents are  
227 calculated via the law of the wall, using Equations (4) - (5):

$$228 \quad u^* = kU(z) / \text{Ln}(z / z_0) \quad (4)$$

$$229 \quad \tau_b = u^{*2} \rho_w \quad (5)$$

230 where  $U(z)$  is the current velocity measured at a depth of  $z$  meter above the  
231 seabed, we adopt 20 m of  $z$  and chose a current speed of 0.5–1.0 m/s as measured  
232 by Acoustic Doppler Current Profiler (Luick et al., 1994);  $k$  is von Kármán constant,  
233  $0.40 \pm 0.02$  (Bailey et al., 2014);  $z_0$  is reference height related to the seabed, for  
234 muddy seabed is estimated to be c. 0.2 mm (Soulsby, 1983).

235

## 236 4. RESULT

237 We divide the Gippsland Basin into Northern, Central, and Southern regions based on  
238 geographical position and seabed morphology (Figure 3A, 3B). The continental shelf of  
239 the Central region extends seaward for approximately 70 km with an average dip of  
240  $0.8^\circ$  then abruptly steepens to  $8.8^\circ$  in the slope (Figure 3C). The water depth of the  
241 Central region ranges from 0-500 m on the shelf and from 500-2000 m on the slope  
242 (Figure 3A). Below we describe the seabed geomorphology and the major sedimentary

243 environments from the shelf to the slope in the Central region of the Gippsland Basin.

244

#### 245 4.1 Seabed geomorphology of the shelf area

246 **Observation:** The Central region is characterized by an erosional seabed (Figures 4A,  
247 4B). On the shelf, a set of north-trending scallop-shaped scarps have been observed  
248 near the outer shelf area (Figure 4C). Seismic sections indicate the scallop-shaped  
249 scarps show a clear truncation edge and erosional base surface (termed as basal shear  
250 surface), marking the boundary that differentiates the overlying undeformed strata  
251 from the deformed sediments (Figures 5A, 5B). Downslope (eastward) to the scarps, a  
252 series of sediment wave fields have been observed along the middle part of the outer  
253 shelf (Figure 4B, 4C). Further downslope, the sediment waves are dissected by a set of  
254 irregular discontinuous concave-downslope scours that occur at the southwestern  
255 part of the shelf (Figures 4B, 4C). In the seismic section, the scours range from 1.2-1.7  
256 km in width, 1.7-3.4 km in length (spacing), from 80-200 m in depth, and with an  
257 aspect ratio (wavelength/height) from 167-221 (Figure 5C). These scours are normally  
258 characterized by truncated, steep lee sides and gentle, slightly upslope-dipping stoss  
259 sides (Figure 5C). Buried step-like bedforms are observed beneath seabed scours (see  
260 insert figure in Figure 5C). The buried bedforms contain sub-parallel, relatively high-  
261 amplitude seismic reflections, and show upslope migration by erosion in the lee side  
262 and deposition in the stoss side (Figure 5C).

263

264 Further NE, three sets of scours aligned in distinctive or discontinuous channel-shaped

265 depressions have been observed in the centre part of the shelf (Figure 4C). The crests  
266 of these scours are consistently oriented approximately north-south, being confined  
267 in the axis of channel-shaped morphology (Figure 4C). Seismic sections cutting along  
268 the thalweg of the channel-shaped depressions show a series of bedforms that form a  
269 train of steps and stretch over a distance of 10-16 km (Figures 5D, 5E). These bedforms  
270 range from 0.2-0.7 km in width, 0.9-1.2 km in wave length, 20-60 m in wave height,  
271 and with aspect ratio from 46-167 (Figures 5D, 5E). A single bedform is characterized  
272 by a steep scarp indicated by truncated seismic reflections that form the lee side  
273 contrast with a gently, lower relief slope at the stoss side (Figures 5D, 5E).

274

275 Further NE of the shelf, at least two well-developed channels have been observed in  
276 the eastern part of the shelf (Figure 4C). Nevertheless, these channels only extend to  
277 the shelf break, and no clear erosions have been observed within the slope (Figures  
278 4B, 4C). These channels vary from 2–10 km in width, and 100–325 m in depth (Figure  
279 4B). They initially trend SSE and then sharply divert to the NE within a few kilometres  
280 distance across the shelf break, and ultimately run to the slope after passing through  
281 the shelf break (Figures 4B, 4C). A set of longitudinal lineations has been observed on  
282 the southern flank of the channels (Figure 4C). These lineations are c. 8 km long, they  
283 are evenly spaced and predominantly oriented parallel to the channel axis. In the  
284 seismic section, the longitudinal lineations show a stair-shaped cross-sectional  
285 geometry and truncations (Figure 5F).

286

287 **Interpretation:** The scalloped scarps developed near the outer shelf indicate a gradual  
288 broadening over time is likely caused by slope failures (i.e. Lee and Chough, 2001). The  
289 scalloped scarps are thus interpreted as headwall scarps associated with a buried  
290 landslide (Figures 5A, 5B). The scours, scour trains, and channels are developed above  
291 the landslide's basal shear surface, suggesting the landslide is being deposited and  
292 predate these bedforms (Figures 5C-F). The sediment wave fields developed within the  
293 scarps are evident in the presence of downslope currents (i.e. Fildani et al., 2006). The  
294 asymmetrical cross-sectional geometry, large aspect ratio, and upslope migration  
295 trend indicate the scours are erosional cyclic steps (or cyclic scours) that are carved by  
296 downslope flowing supercritical currents (Figure 5C; Fildani et al., 2006; Kostic, 2011).  
297 Scours aligned within the channel template are interpreted as erosional cyclic step  
298 trains, which may indicate an incipient channel formation (i.e. Taki and Parker, 2005;  
299 Fildani et al., 2006; Fildani et al., 2013; Zhong et al., 2015). The buried step-like  
300 bedforms are interpreted as partially depositional cyclic steps, formed when sediment  
301 erosion on the lee side is less than sediment deposition on the stoss side (Slootman  
302 and Cartigny, 2020). The presence of the partially depositional cyclic steps suggests  
303 that the downslope flowing currents were active in the Central region for an extended  
304 period of time.

305

306 The channel's diversion near the shelf edge could be a result of the Westerly wind-  
307 induced Ekman transport flow (ETF), which follows a NE-NNE direction, interacting  
308 with the sedimentary systems along the edge of the continental shelf (Mitchell et al.,

309 2007a). The EAC is less likely to contribute to the deviation of the channel axis, as it  
310 separates from the coast approximately between 30°S and 32°S, splitting into eddy-  
311 dominated southern and eastern extensions (Cetina-Heredia et al., 2014; Oke et al.,  
312 2019). The major eddies are anticlockwise, and therefore, the channel courses should  
313 be diverted to the southeast direction, which is opposite to our observation.

314

315 The longitudinal lineations developed within the channels are interpreted as  
316 sedimentary furrows similar to those observed in other submarine settings (i.e. Wynn  
317 and Stow, 2002; Puig et al., 2008). Studies of furrows show that these features were  
318 formed due to recurring, stable, and directional currents (i.e. turbidity currents)  
319 erosion through time (e.g. Flood, 1983; Puig et al., 2008). The presence of furrows in  
320 this study suggests that the ambient downslope flowing currents may have strong and  
321 persistent energy (Flood, 1983). The sole appearance of furrows on the channel's  
322 southern flank suggests that the downslope flowing currents preferential arrival across  
323 the southern channel flank.

324

## 325 4.2 Seabed geomorphology of the slope area

326 **Observation:** Near the upper slope, gullies and landslide scarps are widely distributed  
327 on the slope between water depths 700 to 2000 m (Figure 6). The gullies extend  
328 several kilometres from the upper slope to the lower slope, terminating as the slope  
329 angle decreases and intersects with the Bass Canyon head (Figures 4B, 6). The gullies  
330 are straight and oriented to the dip direction of the slope, characterized by linear



331 morphology, rounded heads and narrow bodies in plain view (Figure 6). Small failures  
332 and slide scarps are evident within or around the edges of the gullies. In the seismic  
333 section, these gullies are V-shaped, and have a relatively flat base reflection with clear  
334 erosive truncation along the sidewalls (Figure 7A). The gully sidewalls have a relief  
335 (incision depth) of 110-230 m, and a width of 120-280 m (Figure 7A). The landslide  
336 scarps roughly dip from NNE to SSW, with widths ranging from c. 4 km to 7km (Figure  
337 6). In seismic sections, these scarps show a stair-shape, backward (i.e. landward)  
338 dipping geometry (Figure 7B).

339

340 Near the lower slope, scours that are aligned in train and parallel to the slope dip  
341 direction have been observed within the gullies and on the inter-gully ridges (Figure  
342 6). Seismic sections cutting along the thalweg of the scour trains show that they are  
343 characterized by steep and erosional lee sides and gentle stoss sides, similar to the  
344 cyclic steps developed on the shelf (Figures 7B-D). These scours are 0.5-1.3 km in  
345 wavelength, 9-19 m in wave height, and aspect ratio is from 12-40. They are best  
346 developed near the lower slope, where the slope gradient drops from  $9^{\circ}$ - $12^{\circ}$  (near the  
347 upper slope) to  $4^{\circ}$ - $7^{\circ}$  (to the lower slope; Figures 7B-D). Further lower slope, giant  
348 landslide scarps that distribute more than 30 km horizontally are observed near the  
349 lowermost of the slope (Figure 6). In the seismic section, the scarps show clear  
350 truncations that separate the undeformed seabed (upslope) from the deformed  
351 erosional seabed (downslope) (Figures 7B-D).

352

353 **Interpretation:** Near the upper slope, the step-shaped pattern of the scarps suggests  
354 a retrogressive failure mechanism of the landslides (Figure 7B; Wu et al., 2021). As the  
355 landslide is located along the shelf edge, where cyclic wave loading can constantly  
356 rework seabed sediments. This process may account for a potential trigger mechanism  
357 leading to slope failure (i.e. Marshall et al., 1978; Bea et al., 1983). The gullies clearly  
358 incise into the landslides, suggesting that they post-date the slope failures (Figure 6).  
359 The linear gullies are interpreted as the conduits for gravity flows to transport  
360 sediment to deeper waters (Micallef and Mountjoy, 2011; Lonergan et al., 2013). The  
361 V-shaped head geometry indicates the origin of the gullies is associated with  
362 downslope gravity-driven currents (i.e. debris flow and turbidity current; Farre et al.,  
363 1983; Gales et al., 2012). Successive small failures are exhibited on the gully ridges,  
364 which is indicative of a gradual widening of the gullies (Post et al., 2022). The scour  
365 trains developed within the gullies and on the inter-gully ridges are interpreted as  
366 cyclic steps, similar to their counterparts developed on the shelf (i.e. Fildani et al.,  
367 2006). The presence of cyclic steps suggests that the slope area is also a supercritical  
368 flow regime-dominated environment, and the erosion by supercritical currents might  
369 play a role in the gully's initiation and evolution (i.e. Noormets et al., 2009; Gales et al.,  
370 2012).

371

372 Our observation suggests that cyclic steps are scarce on the upper slope, where the  
373 slope gradient is steeper ( $9^{\circ}$ - $12^{\circ}$ ), but prominent on the lower slope, where the slope  
374 gradient is relatively gentle ( $4^{\circ}$ - $7^{\circ}$ ) (Figures 7B-D). The discrepancy of the cyclic steps

375 on the upper slope can be explained as the higher slope gradient can cause the  
376 overflowing currents to have a faster velocity, thereby suppressing their ability to  
377 decelerate and undergo internal hydraulic jumps (Kostic, 2011; Zhong et al., 2015). Due  
378 to the higher flow velocity (therefore more energetic), erosional scours and  
379 truncations are common on the upper slope (Figures 7C, 7D). Further downslope,  
380 cyclic steps preferentially form near the lower slope area (Figures 7B-D), suggesting  
381 the transition from high slope gradients to low slope gradients could promote the  
382 formation of the cyclic steps (i.e. Covault et al., 2017; Fildani et al., 2021). The  
383 construction of cyclic steps has led to the formation of local high topographies near  
384 the distal side of the lower slope (Figures 7B-D). These local topographic highs can  
385 form 12°-22° slopes and range from 70-130 m high, leaving a series of spatially  
386 evacuated accommodations near the distal edge of the lower slope (Figures 7B-D).  
387 These evacuated accommodations can reduce the lower slope's lateral confining  
388 pressure, thus increasing seabed instability (Bull et al., 2009). This can be evidenced  
389 by the giant submarine landslides occurring immediately adjacent to, and continuous  
390 headwall scarps developing near the distal side of the local topographic highs (Figures  
391 7B-D). Therefore, we indicate that the local topographic highs can act as landslide-  
392 susceptible structures that ultimately prime slope failures.

393

#### 394 4.3 Piston core and grain size analysis

395 **Observation:** Facies-1 can be observed from the shelf and slope (core #1-4 and 6;  
396 Figure 4B). On the shelf, Facies-1 are observed within the headwall scarps of the buried

397 submarine landslide (Figure 4B). Facies-1 is normally graded, moderately to well-  
398 sorted, and contains coarse-grained sand (predominately near the lower part) with a  
399 sharp top surface and an erosional base surface (Figure 8A). Facies-1 collected from  
400 the slope area suggests this facies is internally structureless and contains shelf-  
401 restricted bioclasts (core #4 and 6; Figure 4B). Facies-2 can be observed from the  
402 upper-lower slope (core #5 and 6; Figure 4B). Facies-2 contains sand- and silt-sized  
403 bioclasts, quartz and siliciclastic clay. Core observation indicates it is poorly sorted,  
404 matrix-supported and often organic-rich (Figure 8B). It also has decimetre-thick  
405 bedding with gradational contacts with bioturbation observed (Figure 8B).

406

407 There are significant differences in grain size distributions between sediment samples  
408 collected outside (west) and within (east) the headwall scarps associated with the  
409 buried landslide (Figure 8C). Sediment samples collected upslope (west) of the  
410 headwall scarps show fine-to-medium sand grain size, and the predominant particle  
411 diameter is between 65  $\mu\text{m}$  and 2 mm (Figure 8C). In comparison, sediment sample  
412 collected within the headwall scarps exhibits sharp grain size variations (Figure 8C).  
413 Specifically, the sediment has an average particle diameter exceeding 2 mm and  
414 consists primarily of coarse-grained gravel.

415

416 **Interpretation:** The erosional base surface, coarse-grained, normally graded, and  
417 internally structureless nature of Facies-1 is a typical indicator of Bouma Ta-typed  
418 turbidites, which are primarily formed by down slope transported turbidity currents

419 (Bouma, 1962). The abundance of shelf-restricted bioclasts observed from the slope  
420 suggests these turbidites originated from the shelf. Therefore, we interpret Facies-1 as  
421 turbidites formed by turbidity currents sourced from the continental shelf. The fine-  
422 grained and organic-rich nature of Facies-2 suggests it is deposited under a low energy  
423 condition. We interpret Facies-2 as representing the background slope environment  
424 (Mitchell et al., 2007b).

425

426 BCC is the dominant oceanographic process on the shelf of the central Gippsland Basin  
427 (Mitchell et al., 2007b), considering the minimum (c. 0.5 m/s) and maximum (c. 1.0  
428 m/s) speed of the BCC (Luick et al., 1994), the sediment grain size that is smaller than  
429  $639 \mu\text{m}$  and  $2.036 \text{ mm}$  would be motional, respectively (Figure 8D). The BCC is  
430 therefore capable of entraining most sediment calibres from the seabed (Figure 8C)  
431 and of forming dense, bottom nepheloid layers during transportation, as suggested by  
432 previous monitoring studies (i.e. Godfrey et al., 1986). The sudden increase in grain  
433 size collected within the headwall scarps suggests a highly turbulent and energetic  
434 flow that is capable of carrying coarse-grained sediments is active (Postma and  
435 Cartigny, 2014). Core analyses conducted in the same area indicate this highly  
436 turbulent and energetic flow is downslope transported turbidity current. Thus, the  
437 significant change in grain size may be attributed to the transition from along-shelf  
438 transported BCC to downslope transported turbidity current, and the transformation  
439 process occurs adjacent to the headwall scarps of the buried landslide.

## 440 5. DISCUSSION

### 441 5.1 Turbidity current: the dominant sedimentary process in central 442 Gippsland Basin

443 The seismic interpretations reveal a continued presence of cyclic steps throughout the  
444 outer shelf and slope areas (Figures 4C and 6), which indicate a continuing role of  
445 downslope-transported supercritical currents in sculpting and remoulding the seabed  
446 in the central Gippsland Basin (i.e. Fildani et al., 2006; Kostic, 2011; Zhong et al., 2015).

447 Published studies suggest that the overriding flow that creates cyclic steps is  
448 supercritical currents with alternating transformation between supercritical and  
449 subcritical flow through hydraulic jumps (i.e. Zhong et al., 2015; Covault et al., 2017;  
450 Fildani et al., 2021). Core observation and grain size analyses have confirmed this  
451 interpretation, as coarse-grained, Ta-typed turbidites are the major facies, indicating  
452 the presence of high-intensity downslope-traversing turbidity currents (Figures 8A, 8C;  
453 Bouma, 1962). Additionally, recent publications indicate that Ta-typed turbidites can  
454 be formed by hydraulic jump-related rapid sedimentation, often associated with high-  
455 energy supercritical turbidity currents (Figure 8A; i.e. Postma and Cartigny, 2014).  
456 Therefore, by combining the results from seismic interpretation, core observation, and  
457 grain size analyses, we interpret that turbidity currents are an important sedimentary  
458 process in the central Gippsland Basin.

459

### 460 5.2 The initiation of turbidity current: transformation from the dense shelf 461 water cascade

462 The origin of turbidity currents has been attributed to three main processes,  
463 transformation from the slope failures, hyperpycnal flows from onshore fluvial input  
464 or subglacial meltwater, and oceanographic processes generated flows near the  
465 shelf edge (Piper and Normark, 2009; Talling et al., 2013). In Gippsland Basin, the  
466 Central region has been completely disconnected from onshore drainage systems  
467 since the Pliocene (Mitchell et al., 2007b), and no modern submarine landslides (only  
468 buried landslide; Figure 5B) are observed in the central shelf. Therefore, slope failures  
469 and onshore fluvial input cannot contribute to the initiation of turbidity currents.  
470 Oceanographic processes including storms, tides, and internal waves may play a role  
471 in resuspending seabed sediments and igniting episodic flows. Nevertheless, as they  
472 occur periodically in most circumstances and their influence is often multi-directional,  
473 they thus lack the ability to generate recurring and stable currents. This contrasts with  
474 our observations, where the erosional features developed on the shelf are inferred to  
475 reflect a recurring, directionally stable flow that is sufficiently strong to erode the  
476 seabed (i.e. Figures 4C, 5C-F). BCC is the primary oceanographic process active on the  
477 shelf of the Central Gippsland Basin (Mitchell et al., 2007b), and it could be a  
478 reasonable cause of turbidity currents. The following sections will examine the  
479 processes involved in this current transformation and examine how turbidity currents  
480 can be maintained during transportation.

481

482 As BCC propagates along and cascades across the continental shelf of the Gippsland  
483 Basin, the sediment entraining process has allowed a density contrast near the bottom

484 of the BCC from the surrounding seawater, forming dense, bottom nepheloid layers  
485 that hover above the seabed (Figures 9A, 9B; Godfrey et al., 1980; Mitchell et al.,  
486 2007b). An equilibrium condition could have remained when BCC flows within a  
487 relatively smooth and flat (c.  $0.8^\circ$ ) shelf region, until it flows into the area affected by  
488 the pre-existing landslide. The headwall scarps of the landslide are 40-70 m deep and  
489 are characterized by a steep gradient ( $7^\circ$ - $10^\circ$ ), which has caused local seabed  
490 depressions and slope gradient variation (Figures 9B, 9C). When the bottom nepheloid  
491 layer moves across and flows over these headwall scarps, a sudden increase in slope  
492 gradient could breach the flow equilibrium condition and enhance the shear stress  
493 (thus entraining capacity) and flow velocity (Ogston et al., 2008; Traer et al., 2012;  
494 Traer et al., 2018). Consequently, the headwall scarps can cause the dense nepheloid  
495 layers to split and sink (Figure 9C). The denser layer would subsequently hover over  
496 the seabed and potentially accelerate when traversing the scarps (Figure 9C).  
497 Accelerating flows could cause additional perturbations and entrain more sediment,  
498 and ultimately ignite a turbidity current (Figure 9C; i.e. Parker et al., 1986; Ogston et  
499 al., 2008). The headwall scarps on the shelf extend over 70 km along the BCC's  
500 transport direction (Figures 3A and 9A), which allows the above-mentioned process to  
501 continue and sediments to remain suspended as the BCC moves. As sediments are  
502 continuously resuspended, they serve as a recurrent source of turbidity current  
503 ignition. Therefore, we summarize on the continental shelf the landslide emplacement  
504 first, then cascading water opportunistically uses the headwall scarps as a  
505 'perturbation point' to transform into turbidity currents and lock in place for cyclic



506 steps (Figure 9A). Other oscillatory oceanographic processes, including Westerly wind-  
507 generated strong wave actions and storm-generated currents, may coincide with the  
508 BCC (or act as external forces to enhance the BCC) and simultaneously resuspend large  
509 amounts of seabed unconsolidated sediments and generate downslope flows,  
510 potentially contributing to the initiation of turbidity currents (Figure 9D; Micallef and  
511 Mountjoy, 2011; Talling et al., 2013).

512

513 After ignition, the steep gradient ( $7^{\circ}$ - $10^{\circ}$ ) of the headwall scarps would provide ample  
514 opportunity for turbidity currents to evolve into the Froude supercritical regime  
515 (Figure 9C). Piper et al. (1999) demonstrate a similar process in the Grand Banks,  
516 where a  $6^{\circ}$  scarp can facilitate debris flow to transform into supercritical turbidity  
517 currents. During transportation, the hydraulic jumps could strengthen flow turbulence  
518 by producing large-scale eddies and standing waves within the turbidity current and  
519 promote the erosional process (Mulder and Cochonat, 1996; Traer et al., 2012; Hiscott  
520 et al., 2013). The presence of 10-16 km-long cyclic step trains suggests that the  
521 turbidity currents have high flow intensity and can repeatedly shape the seabed  
522 (Figure 4C). Therefore, we indicate that the ignited turbidity currents are unlikely to  
523 settle from suspension and have strong energy to transport downslope for a long  
524 distance.

525

### 526 5.3 When and where does this transformation occur?

527 The study area is not the only place where such current transformation occurs, similar

528 diagnostics have been found in the SW Adriatic margin and the NW Mediterranean  
529 Seas. The DSWCs in these two places can also entrain seabed sediment and form  
530 bottom-dense nepheloid layers, and therefore, potentially initiate turbidity currents  
531 (see Appendix 3 for quantification details). In the SW Adriatic margin, where DSWC  
532 flows into Gondola Slide's headwall scarp region, the DSWC creates an area of extreme  
533 seabed complexity characterised by several large-scale scours aligned in a channel  
534 template (cf. Figure 7 of Canals et al., 2009). In the Bari Canyon system, Trincardi et al.  
535 (2007) proved that when intense DSWC flows through the canyon head, it can be  
536 captured, confined, and transported in a flow regime similar to that of a turbidity  
537 current. In the NW Mediterranean Seas, when DSWC cascades into and channelizing  
538 through the head of the Cap de Creus Canyon, it carries coarse particles and forms  
539 field of giant furrows and overconsolidated the substrate mud (Puig et al., 2008; Puig,  
540 2017). Additionally, when DSWC cascades into the canyon heads of the Bourcart  
541 Canyon, the current accelerates and transports coarser particles than before entering  
542 the canyon head (Gaudin et al., 2006). All the seabed geomorphologies and erosive  
543 features identified in the above-mentioned studies require directional, stable and  
544 highly energetic processes to develop. Although the published works interpret these  
545 erosional features as being formed by the DSWC (Canals et al., 2006; Puig et al., 2008),  
546 it is highly reasonable that the DSWC interacted with the pre-existing seabed  
547 topographies and transformed into a turbidity current before creating these erosional  
548 bedforms. The transformed turbidity current thus carries coarse material and abrades  
549 the seabed, induces resuspension and generates erosive bedforms.

550

551 Therefore, we note that the transformation of the DSWC into turbidity currents should  
552 be a common process on the outer continental shelves globally. We infer that this  
553 current transformation can occur where the seabed gradient has a sharp increase,  
554 usually caused by the presence of faults and folds associated with submarine  
555 landslides and/or canyons. The newly transformed turbidity currents are competent  
556 to establish erosional conditions and become sufficiently large and energetic to carry  
557 coarse-grained sediments to reach the lower slope and even the basin floor.  
558 Additionally, this current transformation has unravelled the puzzle for the long-  
559 distance transportation ability of the DSWC, since turbidity currents can often extend  
560 hundreds of kilometres and constitute a significant mechanism for sediment transfer  
561 from shallow to deep marine settings (i.e. Pirmez and Imran, 2003).

562

#### 563 5.4 The evolution of seabed geomorphology

564 Cyclic steps and related supercritical bedforms are recognised as fundamentally  
565 important building blocks of seabed geomorphology evolution in many submarine  
566 settings (Fildani et al., 2006; Covault et al., 2017; Fildani et al., 2021). In the Gippsland  
567 Basin, the cyclic steps and cyclic step trains can represent morphodynamic signals for  
568 turbidity current channel initiation (cf. Figure 7 of Fildani et al., 2013; Fildani et al.,  
569 2021). Under the continuous erosion associated with turbidity currents, these cyclic  
570 steps could migrate upslope and focus turbidity currents, gradually coalesce and  
571 eventually become a developed channel (Figure 10A, 10B; Fildani et al., 2013). The

572 channel could further evolve laterally and longitudinally, ultimately forming a mature  
573 submarine drainage network (i.e. canyon) under the maintenance of sediment capture  
574 associated with turbidity currents (Figure 10C). On the slope, the supercritical turbidity  
575 currents have resulted in considerable seabed erosion, generating widespread gullies  
576 that represent an immature drainage system (Figure 10B; Santangelo et al., 2013).  
577 With the continuous downslope transportation of the turbidity currents and other  
578 gravity flows (i.e. submarine landslide), the gullies will act as preferential conduits for  
579 large-scale sediment transfer and may evolve into canyons (Figure 10C; Santangelo et  
580 al., 2013).

581

## 582 6. Implication

### 583 6.1 For biodiversity and carbon sequestration

584 The DSWC often occur in late winter to early spring, at a time synchronous with high  
585 biological production levels (i.e. marine phytoplankton bloom), the DSWC can thus  
586 efficiently transfer significant quantities of minerals, organic material and oxygen,  
587 supplying the functioning of continental shelf ecosystems (Sanchez-Vidal et al., 2008).

588 The transformation from DSWC to turbidity current could act as a fast way of fuelling  
589 and renewing nutrients from the shallow marine to the deeper marine environment  
590 (i.e. water depth > 1000 m). This process could significantly enhance biodiversity in the  
591 slope and abyssal environment (Danovaro et al., 2009; Harris, 2014). On the other  
592 hand, the cascading current can carry huge amounts of organic carbon and store them  
593 in the shallow marine (Canals et al., 2006). The subsequent transformation to turbidity

594 current allows the shallowly stored organic carbon to travel to deeper marine and thus  
595 contribute to submarine carbon sequestration as deeper marine has higher reservoir  
596 potential and carbon is less likely to return to the atmosphere. Therefore, the current  
597 transformation mechanism presented in this study contributes to the ventilation of  
598 intermediate and deep waters in the oceans and has a significant impact on  
599 biogeochemical cycles and carbon sequestration.

600

## 601 6.2 For natural hazard mitigation

602 The emplacement of turbidity currents could break valuable seabed  
603 telecommunications cables that carry >95% of global data (Carter et al., 2014) and  
604 damage submarine pipelines may cause potential hydrocarbon leakage hazards  
605 (Porcile et al., 2020). In 2022, the Australian Government announced new wind farm  
606 construction plans on the Victorian Coast in the Gippsland Basin (the same area as this  
607 study; see from Victorian State Government website). Therefore, we suggest that  
608 future marine spatial planning and offshore constructions should consider a  
609 reasonable band of the buffer zone (e.g. 10-20 km wide; Figure 10C) landward to the  
610 landslide headwall scarps located in the central shelf. We also indicate that new  
611 geological and geophysical datasets (including sedimentary cores, additional 3D  
612 seismic reflection data, crewed submersible dives, and Autonomous Underwater  
613 Vehicles) need to assess modern seabed conditions (oceanographic and  
614 geomorphology), to provide better suggestions for future assessments.

615

616 **7. CONCLUSION**

617 Our results elucidate the dense shelf water cascade (DSWC) can interact with pre-  
618 existing submarine landslides and subsequently transform into (supercritical) turbidity  
619 currents. The newly transformed turbidity currents are an effective seabed sculpting  
620 tool and hugely influenced the modern seabed geomorphology and sedimentation  
621 process. We infer that this current transformation can occur where the seabed  
622 gradient has a sharp increase, usually caused by the presence of faults and folds  
623 associated with submarine landslides and/or canyons. As DSWC is prominent on many  
624 continental margins, we suggest that this current transformation represents an  
625 unappreciated, yet important trigger for turbidity currents on the outer continental  
626 shelves globally.

627

628 **FIGURE CAPTIONS**

629 Figure 1. (A) Occurrence previously documented dense shelf water cascade (DSWC)  
630 around the world. Numbers in each area refer to the location: (1) Eastern Chukchi Sea  
631 shelf, (2) Beaufort Sea shelf, (3) Foxe Basin, northernmost part of Hudson Bay, (4) SW  
632 Greenland margin, (5) Northern gulf of California, (6) North American south-eastern  
633 shelf, (7) Great Bahama Bank, (8) East Greenland Shelf and south of Denmark Strait,  
634 (9) West Spitsbergen shelf, (10) Bear Island Channel, Barents Sea, (11) hindered in  
635 Storfjord, Barents Sea, (12) Skagerrak, eastern flank of the North Sea, (13) Rockall Bank,  
636 North Atlantic Ocean, (14) Celtic Sea shelf, North Atlantic Ocean, (15) Gulf of Lion, NW  
637 Mediterranean Sea, (16) Gondola slide area, Adriatic Sea shelf, (17) Cape Bari, SE

638 Adriatic Sea shelf, (18) Southern Mediterranean Sea shelf, (19) Aegean Sea shelf, (20)  
639 Banc d'Arguin, near Cape Blanc and off the west African coast, (21) Western shelf of  
640 Novaya Zemlya, Barents Sea, (22) shelf of Nansen Basin, Arctic Ocean, (23) North-  
641 eastern Severnaya Zemlya shelf, Laptev Sea, (24) Northern sea of Okhotsk, north-  
642 western Pacific Ocean, (25) Peter the Great Bay, near the Japan Sea continental slope,  
643 (26) NW Australia inner shelf, (27) Shark Bay, western Australia, (28) Great Australian  
644 Bight, southern Australia, (29) Jervis Bay, southern Australia, (30) Bass Strait, south-  
645 eastern Australia, (31) Spencer Gulf, east Australia, (32) The Hikurangi subduction  
646 margin, SE of central New Zealand, (33) The western Ross Sea, Antarctic Ocean, (34)  
647 The Adélie Coast, East Antarctic sector, Antarctic Ocean, (35) Prydz Bay, East Antarctica,  
648 (36) Southern margin of Weddell Sea shelf, (37) Eastern margin of Weddell Sea shelf,  
649 (38) The southern Ross Sea, Antarctic Ocean. Note that the blue dots are based on the  
650 DSWC global atlas by Ivanov et al. (2004) and the DSWC recorded around Australian  
651 shelves by Mahjabin et al. (2020). The pink dots indicate recently reported (2004–  
652 present) cascading phenomena measured by long-term and high-frequency in situ  
653 measurements globally, see Appendix 2 for the supporting references. (B) Schematics  
654 of the DSWC mechanism showing the formation of intermediate nepheloid layers on  
655 the shelf and the downslope turbidity currents. Adapted from Fohrmann et al. (1998).  
656  
657 Figure 2. (A) The regional map of Australia shows the location of the study area  
658 (indicated in a red polygon) and the oceanographic setting. The trajectories of the main  
659 oceanic currents are represented by white, blue, and yellow dashed lines. LC, Leeuwin

660 Current; SAC, South Australian Current; ZC, Zeehan Current; BCC, Bass Cascade Current;  
661 EAC, East Australian Current. In Gippsland Basin, when the BCC flows through the Bass  
662 Strait during winter, it is further fed by the LC, ZC and the wind stress within the Bass  
663 Strait, jointly transporting Bass Strait water towards the front (Li et al., 2005; Mitchell  
664 et al., 2007b). During summer, though the BCC is less active, strong offshore wind and  
665 tidal activities can further reinforce and transport Bass Strait water eastwards (Godfrey  
666 et al., 1980). (B) Zoom in view of the Gippsland Basin and the Bass Canyon. Note the  
667 north arrow (white) and the yellow box denote the location of the 3D seismic data.  
668 The transportation pathway of the BCC is based on data collected from the  
669 Conductivity, Temperature, and Depth (CTD) sensors adopted during the winter of  
670 1981 by Tomczak (1985). The transportation pathway of the EAC is adopted from  
671 Lavering (1994) and Ridgway and Hill (2009). (C) Temperature profile of the Bass Strait  
672 showing the downward temperature anomalies within the continental shelf and slope.  
673 (D) Temperature profile (potential temperature) in offshore eastern Australia, showing  
674 the depth of the East Australian Current (EAC). The temperature data is from the WOCE  
675 (World Ocean Current Experiment) Hydrographic Program (available at  
676 <https://odv.awi.de/data/ocean>). See Figure 2A for locations.

677

678 Figure 3. (A) 3D view of seabed multibeam bathymetric map of the offshore Gippsland  
679 Basin and Bass Canyon system, showing the main geomorphologic features. (B) Sketch  
680 of Figure 3A, showing the key depositional elements, canyons and distinguished  
681 regional domains. (C) Shelf-to-slope seismic profile showing the Central shelf and slope



682 regions. See Figure 3B for location.

683

684 Figure 4. (A) Seabed structure map generated from the 3D seismic data, showing the  
685 seabed morphology in the Central Region. (B) Dip illumination attribute map  
686 calculated from the 3D seismic data, showing the detailed sedimentary structures of  
687 the Central Region. Note the yellow dots indicate the piston core location. (C) Zoomed-  
688 in view of the continental shelf in the Central Region, emphasizing the sediment waves,  
689 cyclic steps and channels. See Figure 4B for location.

690

691 Figure 5. (A) Seismic dip section cut through the headwall scarps of the landslide. (B)  
692 Seismic longitudinal profile along the axis of the cyclic step train. (C) Seismic  
693 longitudinal profile cutting through the axis of channel-formed cyclic steps. The  
694 inserted schematic map shows a series of idealized asymmetrical cyclic steps and  
695 hypothetical densimetric Froude number ( $Fr$ ) variability. Within a single bedform, the  
696 supercritical flow creates a hydraulic jump ( $Fr_d > 1$ ) at the base of the lee side and  
697 transfers to subcritical flow ( $Fr_d < 1$ ) at the stoss side. Subsequently, the subcritical flow  
698 reaccelerates to supercritical flow again down to the lee side of the next bedform. The  
699 schematic map was modified by Cartigny et al. (2011). (D) Seismic longitudinal profile  
700 cutting through the axis of channel-formed cyclic steps. (E) Seismic cross-sectional  
701 profile cutting through the channels; note the stair-shaped erosional characteristics of  
702 furrows developed on the channel sidewalls. See Figure 4C for locations.

703

704 Figure 6. Zoomed-in view of the continental slope in the Central Region, emphasizing  
705 the landslides and gullies. See Figure 4B for location.

706

707 Figure 7. (A) Seismic section illustrating gullies' cross-sectional geometries. (B) Seismic  
708 dip section cutting along the gully ridge. (C) Seismic dip section cutting along the gully  
709 ridge. (D) Seismic dip section cutting within the gully and along its thalweg. See Figure  
710 6 for locations.

711

712 Figure 8. (A) Core sketch generated based on piston core report from the central region  
713 of the Gippsland Basin, showing the cross-section of the Facies-1. (B) Core sketch  
714 generated based on piston core report, showing the cross-section of Facies-2. Core  
715 locations in Figure 4B. (C) Grain size distribution in the Central area of the Gippsland  
716 Basin. The blue arrow indicates the transport direction of the BCC. (D) The sediment  
717 motion threshold curve under the given values of sediment grain size and BCC current  
718 speed.

719

720 Figure 9. (A) The 3D view of the Central Region, showing the seabed morphological  
721 structures and major current pathways. (B) Schematic 2D plain view of the Central  
722 shelf, illustrating the location of headwall scarps, the pathway of the BCC and its  
723 associated supercritical turbidity currents. See Figure 9A for location. (C) Schematic  
724 cross-section showing the transformation from BCC to turbidity currents. See the text  
725 for explanations and Figure 9B for location. (D) Schematic cross-section depicting the

726 combined influence of the Westerly Wind, internal waves, and tide-induced sediment  
727 resuspension and turbidity current initiation. See Figure 9A for location.

728

729 Figure 10. Schematic of seabed geomorphology evolution processes in the Central  
730 Region of the Gippsland Basin. (A) Shelf: the transformation of the Bass Cascading  
731 Current (BCC) into turbidity currents; Slope: the generation of scarps caused by wave  
732 activities near the upper slope. (B) Shelf: The formation of the sedimentary structures  
733 caused turbidity currents; Slope: The initiation of gullies and the formation of the  
734 landslides on the upper slope. (C) Shelf: The evolution from cyclic steps into channels  
735 and canyons; Slope: landslide initiation near the lower slope. Note that the buffer zone  
736 indicates a stable seabed not influenced by the current transformation process or the  
737 ignited turbidity current.

738 REFERENCE

- 739 Bouma, A.H.P.H.K.F.P.S., 1962. Sedimentology of some Flysch deposits : a graphic approach to  
740 facies interpretation. Elsevier, Amsterdam
- 741 Boland, F., 1971. Temperature-salinity anomalies at depths between 200m and 800m in the  
742 Tasman sea. *Marine and Freshwater Research* 22, 55-62.
- 743 Marshall, N., Stanley, D., Kelling, G., 1978. Large storm-induced sediment slump reopens an  
744 unknown Scripps submarine canyon tributary. *Sedimentation in submarine canyons, fans, and  
745 trenches: Stroudsburg, Pennsylvania, Hutchinson and Ross*, 73-84.
- 746 Godfrey, J., Jones, I., Maxwell, G., Scott, B., 1980. On the winter cascade from Bass Strait into  
747 the Tasman Sea. *Marine and Freshwater Research* 31, 275-286.
- 748 Bea, R.G., Wright, S.G., Sircar, P., Niedoroda, A.W., 1983. Wave-induced slides in south pass  
749 block 70, Mississippi Delta. *Journal of Geotechnical Engineering* 109, 619-644.
- 750 Farre, J.A., McGregor, B.A., Ryan, W.B., Robb, J.M., 1983. Breaching the shelfbreak: passage  
751 from youthful to mature phase in submarine canyon evolution.
- 752 Flood, R.D., 1983. Classification of sedimentary furrows and a model for furrow initiation and  
753 evolution. *Geological Society of America Bulletin* 94, 630-639.
- 754 Soulsby, R.L., 1983. The bottom boundary layer of shelf seas, Elsevier oceanography series.  
755 Elsevier, pp. 189-266.
- 756 Tomczak, 1985. The Bass Strait water cascade during winter 1981. *Continental Shelf Research*  
757 4, 255-278.
- 758 Godfrey, J., Vaudrey, D., Hahn, S., 1986. Observations of the shelf-edge current south of  
759 Australia, winter 1982. *Journal of Physical Oceanography* 16, 668-679.
- 760 Parker, G., Fukushima, Y., Pantin, H.M., 1986. Self-accelerating turbidity currents. *Journal of  
761 Fluid Mechanics* 171, 145-181.
- 762 Tomczak, M., 1987. The Bass Strait water cascade during summer 1981–1982. *Continental  
763 Shelf Research* 7, 561-572.
- 764 Rahmanian, V., Moore, P., Mudge, W., Spring, D., 1990. Sequence stratigraphy and the habitat  
765 of hydrocarbons, Gippsland Basin, Australia. *Geological Society, London, Special Publications*  
766 50, 525-544.
- 767 Colwell, J.B., Constantine, A.E., Willcox, J.B., 1993. Regional structure of the Gippsland Basin:  
768 interpretation and mapping of a deep seismic data set. Australian Geological Survey  
769 Organisation.
- 770 Lavering, I.H., 1994. Marine environments of Southeast Australia (Gippsland Shelf and Bass  
771 Strait) and the impact of offshore petroleum exploration and production activity. *Marine  
772 georesources & geotechnology* 12, 201-226.
- 773 Luick, J.L., Ka, R., Tomczak, M., 1994. On the formation and spreading of the Bass Strait cascade.  
774 *Continental Shelf Research* 14, 385-399.
- 775 Mulder, T., Cochonat, P., 1996. Classification of offshore mass movements. *Journal of  
776 Sedimentary research* 66, 43-57.
- 777 Soulsby, R., 1997. Dynamics of marine sands.
- 778 Fohrmann, H., Backhaus, J.O., Blaume, F., Rumohr, J., 1998. Sediments in bottom-arrested  
779 gravity plumes: Numerical case studies. *Journal of Physical Oceanography* 28, 2250-2274.
- 780 Hill, P., Exon, N., Keene, J., Smith, S., 1998. The continental margin off east Tasmania and  
781 Gippsland: structure and development using new multibeam sonar data. *Exploration  
782 Geophysics* 29, 410-419.
- 783 Piper, D.J., Cochonat, P., Morrison, M.L., 1999. The sequence of events around the epicentre  
784 of the 1929 Grand Banks earthquake: initiation of debris flows and turbidity current inferred  
785 from sidescan sonar. *Sedimentology* 46, 79-97.
- 786 Lee, S., Chough, S., 2001. High-resolution (2–7 kHz) acoustic and geometric characters of

787 submarine creep deposits in the South Korea Plateau, East Sea. *Sedimentology* 48, 629-644.  
788 Exon, N., Hill, P., Partridge, A., Chaproniere, G., Keene, J., 2002. Cretaceous volcanogenic and  
789 Miocene calcareous strata dredged from the deepwater Gippsland Basin on RV Franklin  
790 Research Cruise FR11/98. *Geoscience Australia Record* 7.  
791 Wynn, R.B., Stow, D.A., 2002. Recognition and interpretation of deep-water sediment waves-  
792 implications for palaeoceanography, hydrocarbon exploration and flow process interpretation  
793 (Introduction to special issue). *Marine Geology* 192, 1-3.  
794 Pirmez, C., Imran, J., 2003. Reconstruction of turbidity currents in Amazon Channel. *Marine*  
795 *and petroleum geology* 20, 823-849.  
796 Ivanov, V., Shapiro, G., Huthnance, J., Aleynik, D., Golovin, P., 2004. Cascades of dense water  
797 around the world ocean. *Progress in oceanography* 60, 47-98.  
798 Li, F., Dyt, C., Griffiths, C., Jenkins, C., Rutherford, M., Chittleborough, J., 2005. Seabed  
799 sediment transport and offshore pipeline risks in the Australian southeast. *The APPEA Journal*  
800 45, 523-534.  
801 Taki, K., Parker, G., 2005. Transportational cyclic steps created by flow over an erodible bed.  
802 Part 1. Experiments. *Journal of Hydraulic Research* 43, 488-501.  
803 Canals, M., Puig, P., de Madron, X.D., Heussner, S., Palanques, A., Fabres, J., 2006. Flushing  
804 submarine canyons. *Nature* 444, 354-357.  
805 Fildani, A., Normark, W.R., Kostic, S., Parker, G., 2006. Channel formation by flow stripping:  
806 Large-scale scour features along the Monterey East Channel and their relation to sediment  
807 waves. *Sedimentology* 53, 1265-1287.  
808 Gaudin, M., Berné, S., Jouanneau, J.-M., Palanques, A., Puig, P., Mulder, T., Cirac, P., Rabineau,  
809 M., Imbert, P., 2006. Massive sand beds attributed to deposition by dense water cascades in  
810 the Bourcart canyon head, Gulf of Lions (northwestern Mediterranean Sea). *Marine Geology*  
811 234, 111-128.  
812 Middleton, J.F., Bye, J.A., 2007. A review of the shelf-slope circulation along Australia's  
813 southern shelves: Cape Leeuwin to Portland. *Progress in Oceanography* 75, 1-41.  
814 Mitchell, J., Holdgate, G., Wallace, M., 2007a. Pliocene–Pleistocene history of the Gippsland  
815 Basin outer shelf and canyon heads, southeast Australia. *Australian Journal of Earth Sciences*  
816 54, 49-64.  
817 Mitchell, J., Holdgate, G., Wallace, M., Gallagher, S., 2007b. Marine geology of the Quaternary  
818 Bass Canyon system, southeast Australia: a cool-water carbonate system. *Marine geology* 237,  
819 71-96.  
820 Trincardi, F., Fogliani, F., Verdicchio, G., Asioli, A., Correggiari, A., Minisini, D., Piva, A., Remia, A.,  
821 Ridente, D., Taviani, M., 2007. The impact of cascading currents on the Bari Canyon System,  
822 SW-Adriatic margin (Central Mediterranean). *Marine Geology* 246, 208-230.  
823 Herrmann, M., Estournel, C., Déqué, M., Marsaleix, P., Sevault, F., Somot, S., 2008. Dense water  
824 formation in the Gulf of Lions shelf: Impact of atmospheric interannual variability and climate  
825 change. *Continental Shelf Research* 28, 2092-2112.  
826 Ogston, A.S., Drexler, T.M., Puig, P., 2008. Sediment delivery, resuspension, and transport in  
827 two contrasting canyon environments in the southwest Gulf of Lions. *Continental Shelf*  
828 *Research* 28, 2000-2016.  
829 Puig, P., Palanques, A., Orange, D., Lastras, G., Canals, M., 2008. Dense shelf water cascades  
830 and sedimentary furrow formation in the Cap de Creus Canyon, northwestern Mediterranean  
831 Sea. *Continental Shelf Research* 28, 2017-2030.  
832 Sanchez-Vidal, A., Pasqual, C., Kerhervé, P., Calafat, A., Heussner, S., Palanques, A., Durrieu de  
833 Madron, X., Canals, M., Puig, P., 2008. Impact of dense shelf water cascading on the transfer  
834 of organic matter to the deep western Mediterranean basin. *Geophysical Research Letters* 35.  
835 Bull, S., Cartwright, J., Huse, M., 2009. A subsurface evacuation model for submarine slope  
836 failure. *Basin Research* 21, 433-443.  
837 Canals, M., Danovaro, R., Heussner, S., Lykousis, V., Puig, P., Trincardi, F., Calafat, A.M., de

838 Madron, X.D., Palanques, A., Sanchez-Vidal, A., 2009. Cascades in Mediterranean submarine  
839 grand canyons. *Oceanography* 22, 26-43.

840 Danovaro, R., Canals, M., Gambi, C., Heussner, S., Lampadariou, N., Vanreusel, A., 2009.  
841 Exploring benthic biodiversity patterns and hotspots on European margin slopes.  
842 *Oceanography* 22, 16-25.

843 Noormets, R., Dowdeswell, J., Larter, R.D., Cofaigh, C.Ó., Evans, J., 2009. Morphology of the  
844 upper continental slope in the Bellingshausen and Amundsen Seas—Implications for  
845 sedimentary processes at the shelf edge of West Antarctica. *Marine Geology* 258, 100-114.

846 Piper, D.J., Normark, W.R., 2009. Processes that initiate turbidity currents and their influence  
847 on turbidites: a marine geology perspective. *Journal of Sedimentary Research* 79, 347-362.

848 Ridgway, K., Hill, K., 2009. The East Australian Current.

849 Paull, C.K., Ussler III, W., Caress, D.W., Lundsten, E., Covault, J.A., Maier, K.L., Xu, J., Augenstein,  
850 S., 2010. Origins of large crescent-shaped bedforms within the axial channel of Monterey  
851 Canyon, offshore California. *Geology* 6, 755-774.

852 Cartigny, M.J., Postma, G., Van den Berg, J.H., Mastbergen, D.R., 2011. A comparative study of  
853 sediment waves and cyclic steps based on geometries, internal structures and numerical  
854 modeling. *Marine Geology* 280, 40-56.

855 Kostic, S., 2011. Modeling of submarine cyclic steps: Controls on their formation, migration,  
856 and architecture. *Geosphere* 7, 294-304.

857 Micallef, A., Mountjoy, J.J., 2011. A topographic signature of a hydrodynamic origin for  
858 submarine gullies. *Geology* 39, 115-118.

859 Gales, J., Larter, R., Mitchell, N., Hillenbrand, C.D., Østerhus, S., Shoosmith, D., 2012. Southern  
860 Weddell Sea shelf edge geomorphology: Implications for gully formation by the overflow of  
861 high-salinity water. *Journal of Geophysical Research: Earth Surface* 117.

862 Traer, M., Hilley, G., Fildani, A., McHargue, T., 2012. The sensitivity of turbidity currents to mass  
863 and momentum exchanges between these underflows and their surroundings. *Journal of*  
864 *Geophysical Research: Earth Surface* 117.

865 Fildani, A., Hubbard, S.M., Covault, J.A., Maier, K.L., Romans, B.W., Traer, M., Rowland, J.C.,  
866 2013. Erosion at inception of deep-sea channels. *Marine and Petroleum Geology* 41, 48-61.

867 Hiscott, R.N., Aksu, A.E., Flood, R.D., Kostylev, V., Yaşar, D., 2013. Widespread overspill from a  
868 saline density-current channel and its interaction with topography on the south-west Black  
869 Sea shelf. *Sedimentology* 60, 1639-1667.

870 Lonergan, L., Jamin, N.H., Jackson, C.A.-L., Johnson, H.D., 2013. U-shaped slope gully systems  
871 and sediment waves on the passive margin of Gabon (West Africa). *Marine Geology* 337, 80-  
872 97.

873 Santangelo, M., Gioia, D., Cardinali, M., Guzzetti, F., Schiattarella, M., 2013. Interplay between  
874 mass movement and fluvial network organization: An example from southern Apennines, Italy.  
875 *Geomorphology* 188, 54-67.

876 Talling, P.J., Paull, C.K., Piper, D.J., 2013. How are subaqueous sediment density flows triggered,  
877 what is their internal structure and how does it evolve? Direct observations from monitoring  
878 of active flows. *Earth-Science Reviews* 125, 244-287.

879 Bailey, S.C., Vallikivi, M., Hultmark, M., Smits, A., 2014. Estimating the value of von Kármán's  
880 constant in turbulent pipe flow. *Journal of Fluid Mechanics* 749, 79-98.

881 Carter, L., Gavey, R., Talling, P.J., Liu, J.T., 2014. Insights into submarine geohazards from breaks  
882 in subsea telecommunication cables. *Oceanography* 27, 58-67.

883 Cetina-Heredia, P., Roughan, M., Van Sebille, E., Coleman, M., 2014. Long-term trends in the  
884 East Australian Current separation latitude and eddy driven transport. *Journal of Geophysical*  
885 *Research: Oceans* 119, 4351-4366.

886 Harris, P.T., 2014. Shelf and deep-sea sedimentary environments and physical benthic  
887 disturbance regimes: a review and synthesis. *Marine Geology* 353, 169-184.

888 Postma, G., Cartigny, M.J., 2014. Supercritical and subcritical turbidity currents and their

889 deposits—A synthesis. *Geology* 42, 987-990.

890 Talling, P.J., 2014. On the triggers, resulting flow types and frequencies of subaqueous  
891 sediment density flows in different settings. *Marine Geology* 352, 155-182.

892 Zhong, G., Cartigny, M.J., Kuang, Z., Wang, L., 2015. Cyclic steps along the South Taiwan Shoal  
893 and West Penghu submarine canyons on the northeastern continental slope of the South  
894 China Sea. *Bulletin* 127, 804-824.

895 Covault, J.A., Kostic, S., Paull, C.K., Sylvester, Z., Fildani, A., 2017. Cyclic steps and related  
896 supercritical bedforms: building blocks of deep-water depositional systems, western North  
897 America. *Marine Geology* 393, 4-20.

898 Puig, P., 2017. Dense shelf water cascading and associated bedforms, Atlas of bedforms in the  
899 western mediterranean. Springer, pp. 35-40.

900 Amblas, D., Dowdeswell, J., 2018. Physiographic influences on dense shelf-water cascading  
901 down the Antarctic continental slope. *Earth-Science Reviews* 185, 887-900.

902 O'Brien, P., Mitchell, C., Nguyen, D., Langford, R., 2018. Mass Transport Complexes on a  
903 Cenozoic paleo-shelf edge, Gippsland basin, southeastern Australia. *Marine and Petroleum*  
904 *Geology* 98, 783-801.

905 Traer, M., Fildani, A., Fringer, O., McHargue, T., Hilley, G., 2018. Turbidity current dynamics: 2.  
906 Simulating flow evolution toward equilibrium in idealized channels. *Journal of Geophysical*  
907 *Research: Earth Surface* 123, 520-534.

908 Oke, P.R., Roughan, M., Cetina-Heredia, P., Pilo, G.S., Ridgway, K.R., Rykova, T., Archer, M.R.,  
909 Coleman, R.C., Kerry, C.G., Rocha, C., 2019. Revisiting the circulation of the East Australian  
910 Current: Its path, separation, and eddy field. *Progress in Oceanography* 176, 102139.

911 Villaceros-Robineau, N., Zúñiga, D., Barreiro-González, B., Alonso-Pérez, F., de la Granda, F.,  
912 Froján, M., Collins, C.A., Barton, E.D., Castro, C.G., 2019. Bottom boundary layer and particle  
913 dynamics in an upwelling affected continental margin (NW Iberia). *Journal of Geophysical*  
914 *Research: Oceans* 124, 9531-9552.

915 Mahjabin, T., Pattiaratchi, C., Hetzel, Y., 2020. Occurrence and seasonal variability of Dense  
916 Shelf Water Cascades along Australian continental shelves. *Scientific reports* 10, 1-13.

917 Morrison, A., Hogg, A.M., England, M.H., Spence, P., 2020. Warm Circumpolar Deep Water  
918 transport toward Antarctica driven by local dense water export in canyons. *Science advances*  
919 6, eaav2516.

920 Porcile, G., Bolla Pittaluga, M., Frascati, A., Sequeiros, O.E., 2020. Typhoon-induced megarips  
921 as triggers of turbidity currents offshore tropical river deltas. *Communications Earth &*  
922 *Environment* 1, 1-13.

923 Slooman, A., Cartigny, M.J., 2020. Cyclic steps: Review and aggradation-based classification.  
924 *Earth-Science Reviews* 201, 102949.

925 Fildani, A., Kostic, S., Covault, J.A., Maier, K.L., Caress, D.W., Paull, C.K., 2021. Exploring a new  
926 breadth of cyclic steps on distal submarine fans. *Sedimentology* 68, 1378-1399.

927 Gales, J., Rebesco, M., De Santis, L., Bergamasco, A., Colleoni, F., Kim, S., Accettella, D.,  
928 Kovacevic, V., Liu, Y., Olivo, E., 2021. Role of dense shelf water in the development of Antarctic  
929 submarine canyon morphology. *Geomorphology* 372, 107453.

930 Wu, N., Nugraha, H.D., Zhong, F.G., Steventon, M., 2021. The role of mass-transport complexes  
931 (MTCs) in the initiation and evolution of submarine canyons.

932 Post, A.L., Przeslawski, R., Nanson, R., Siwabessy, J., Smith, D., Kirkendale, L.A., Wilson, N.G.,  
933 2022. Modern dynamics, morphology and habitats of slope-confined canyons on the  
934 northwest Australian margin. *Marine Geology* 443, 106694.

935

936

Figure 1

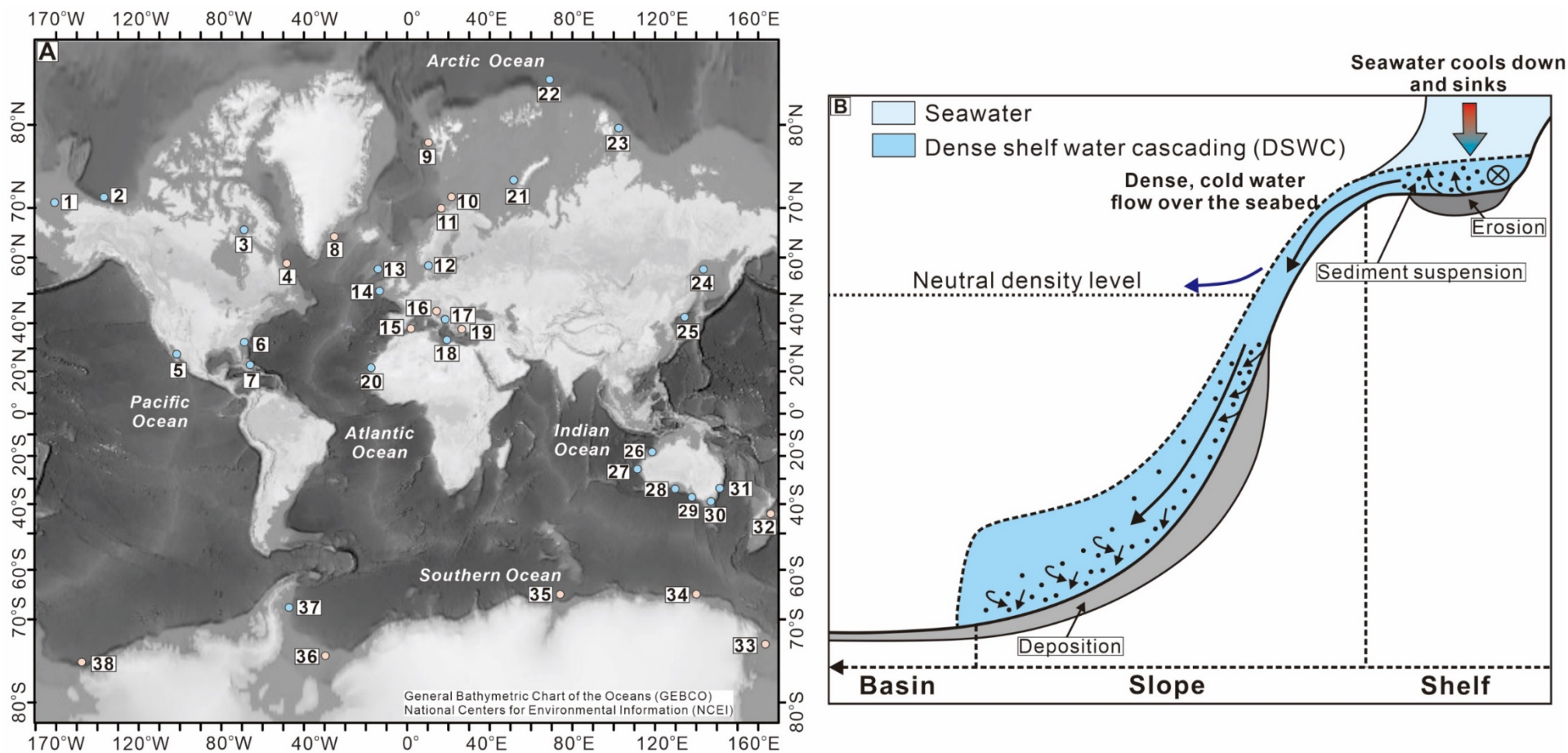




Figure 2

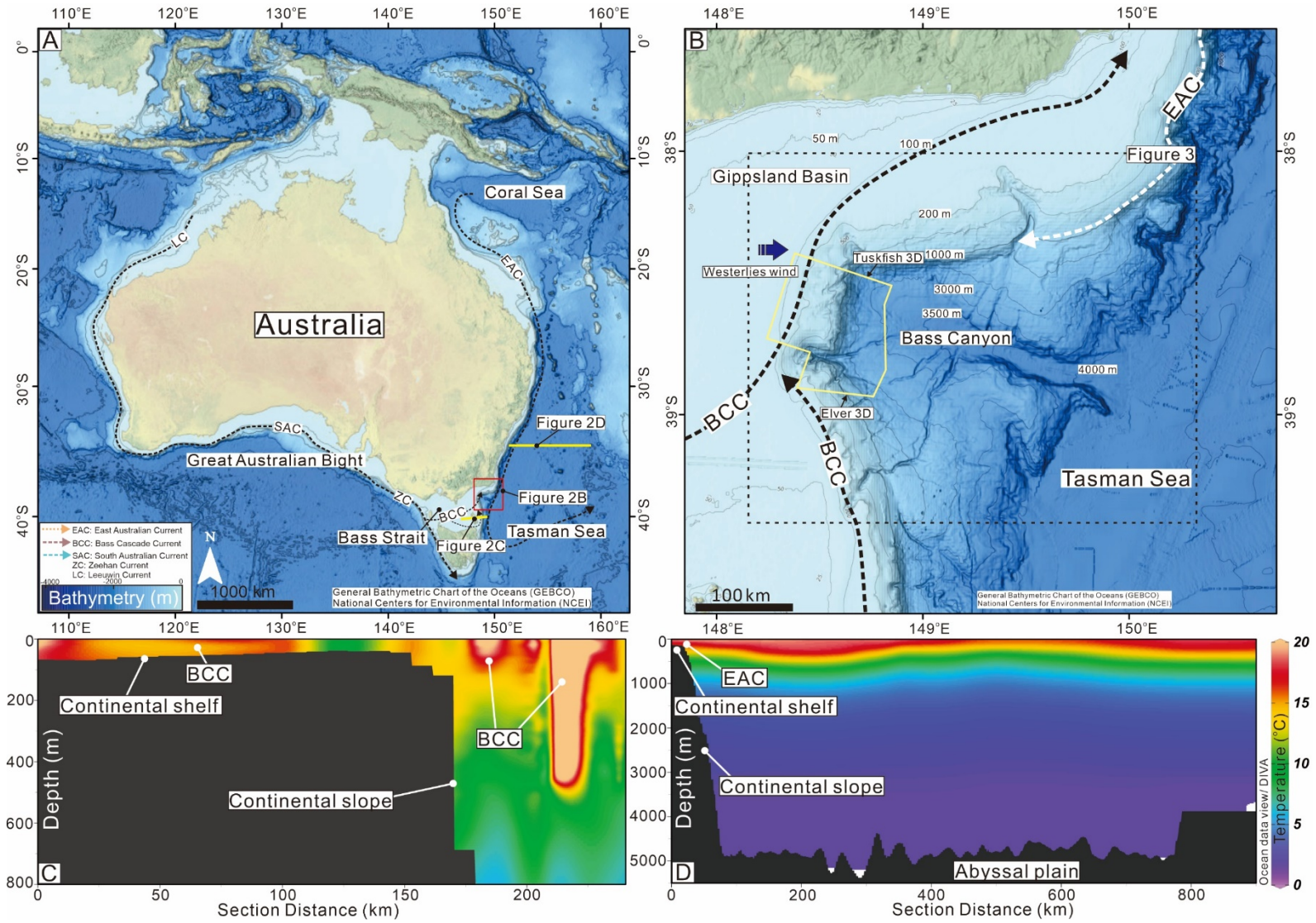


Figure 3

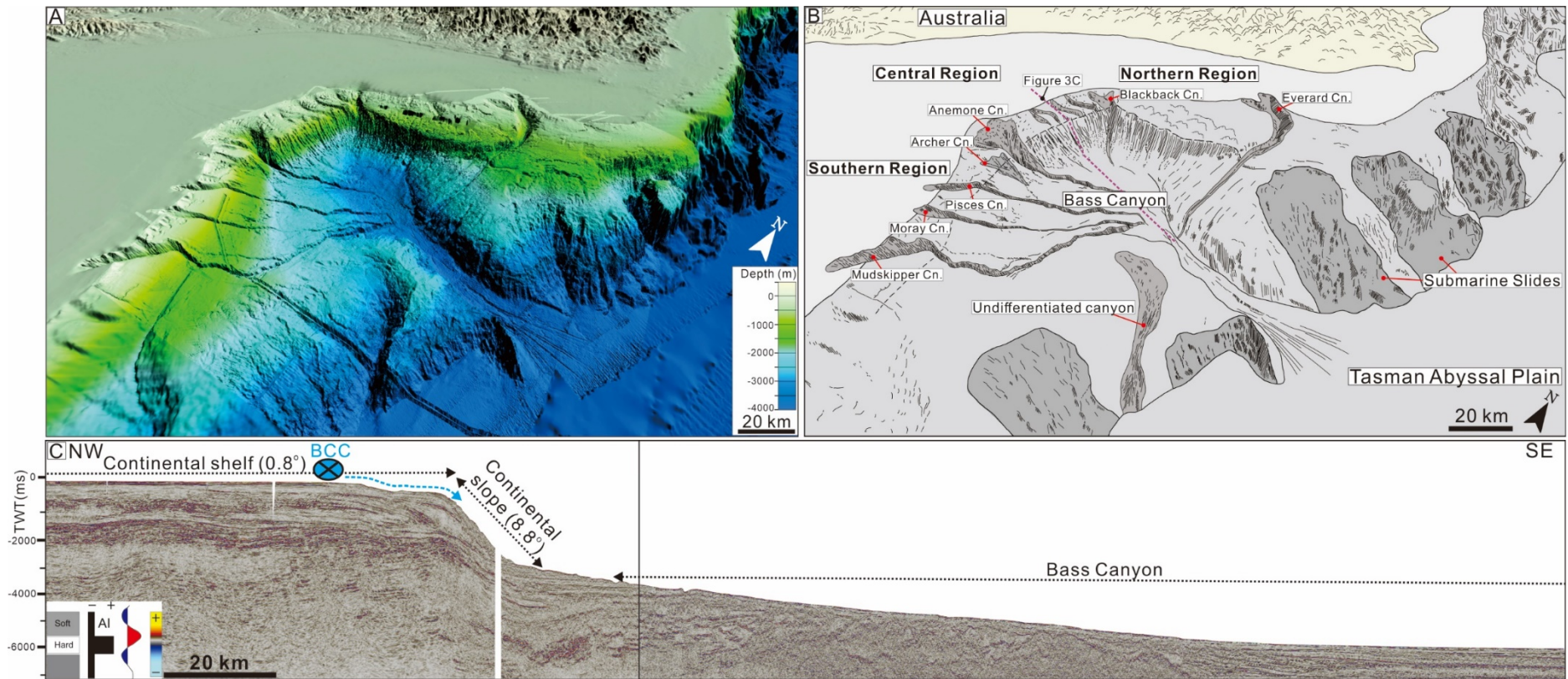
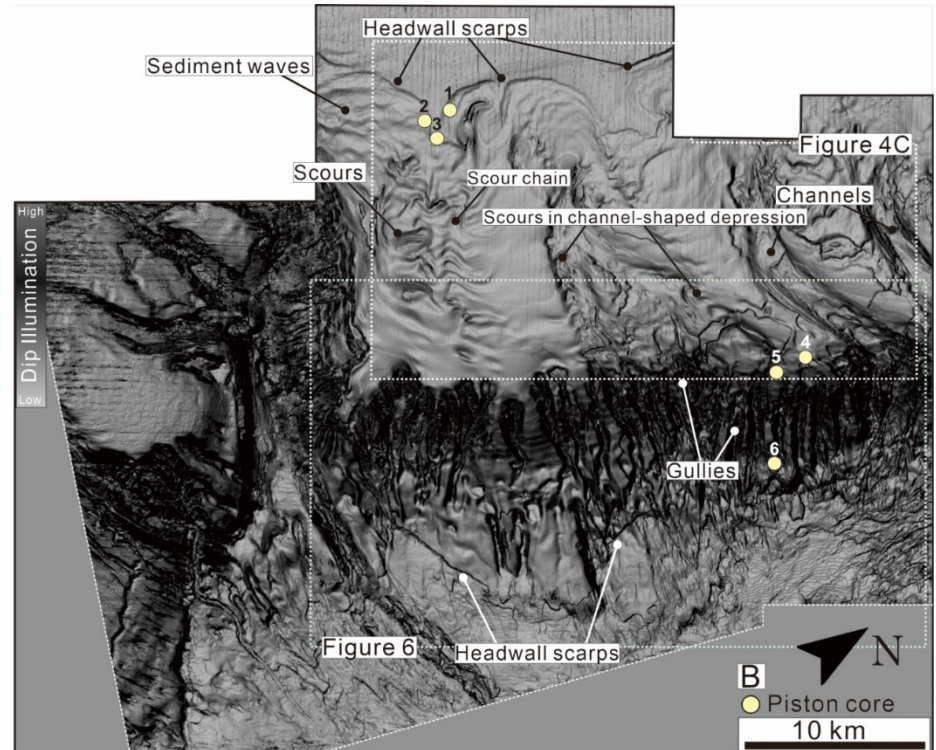
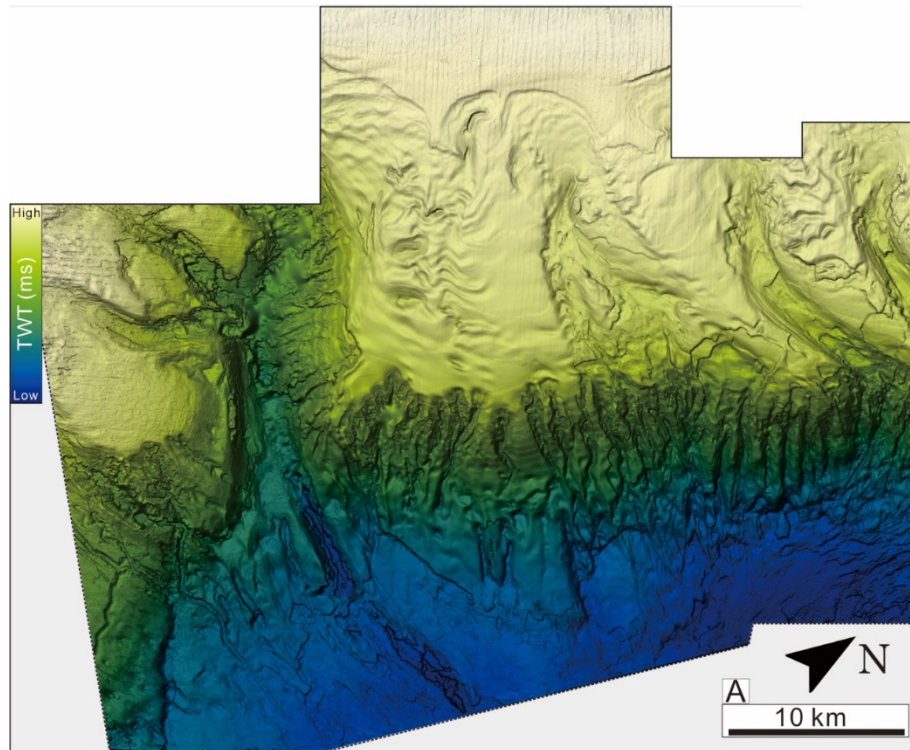
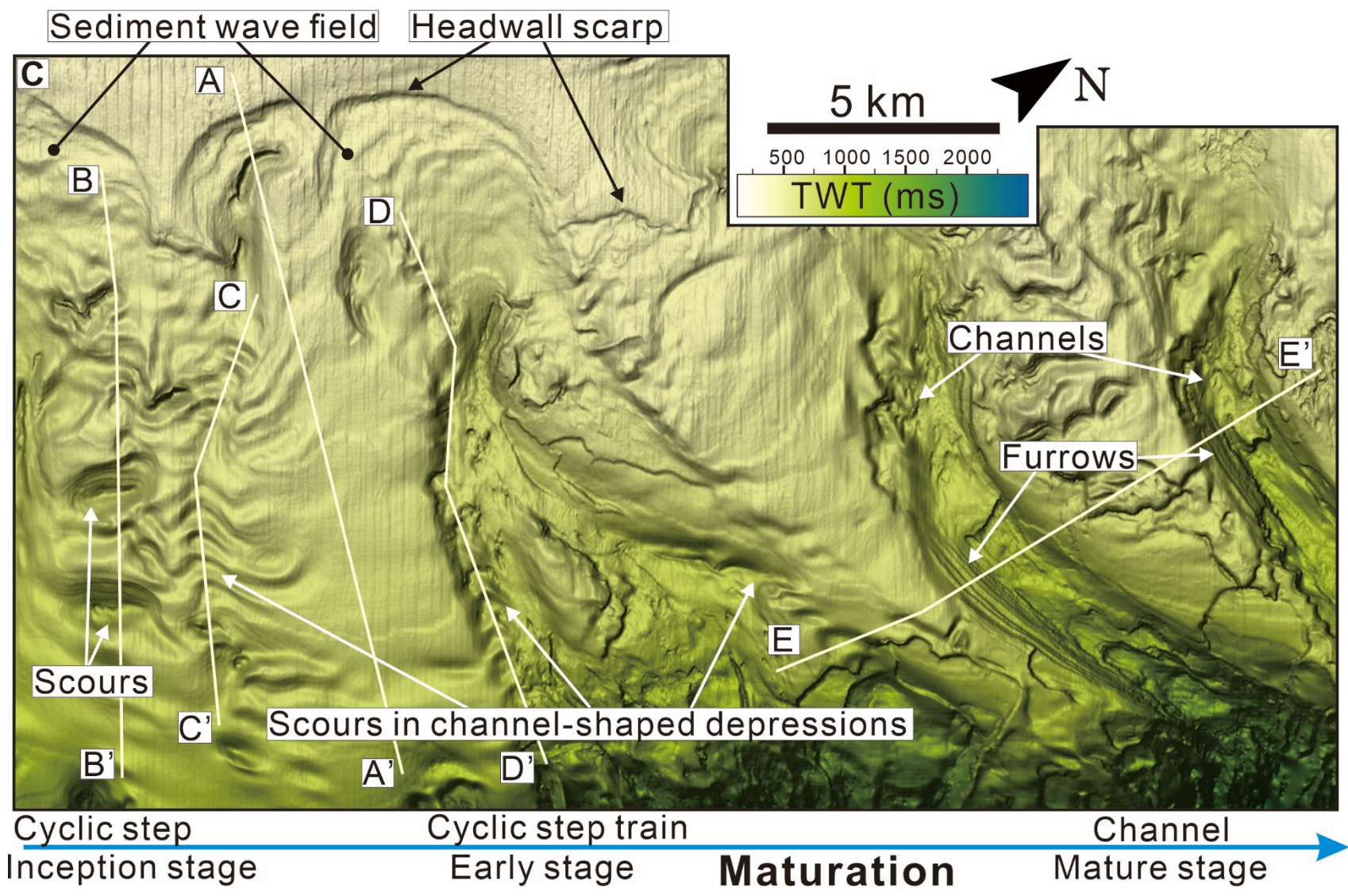


Figure 4





**C**

**A**

**D**

**B**

**C**

**Channels**

**E'**

**Furrows**

**Scours**

**E**

**Scours in channel-shaped depressions**

**B'**

**C'**

**A'**

**D'**

**Cyclic step Inception stage**

**Cyclic step train Early stage**

**Maturation**

**Channel Mature stage**

Figure 5

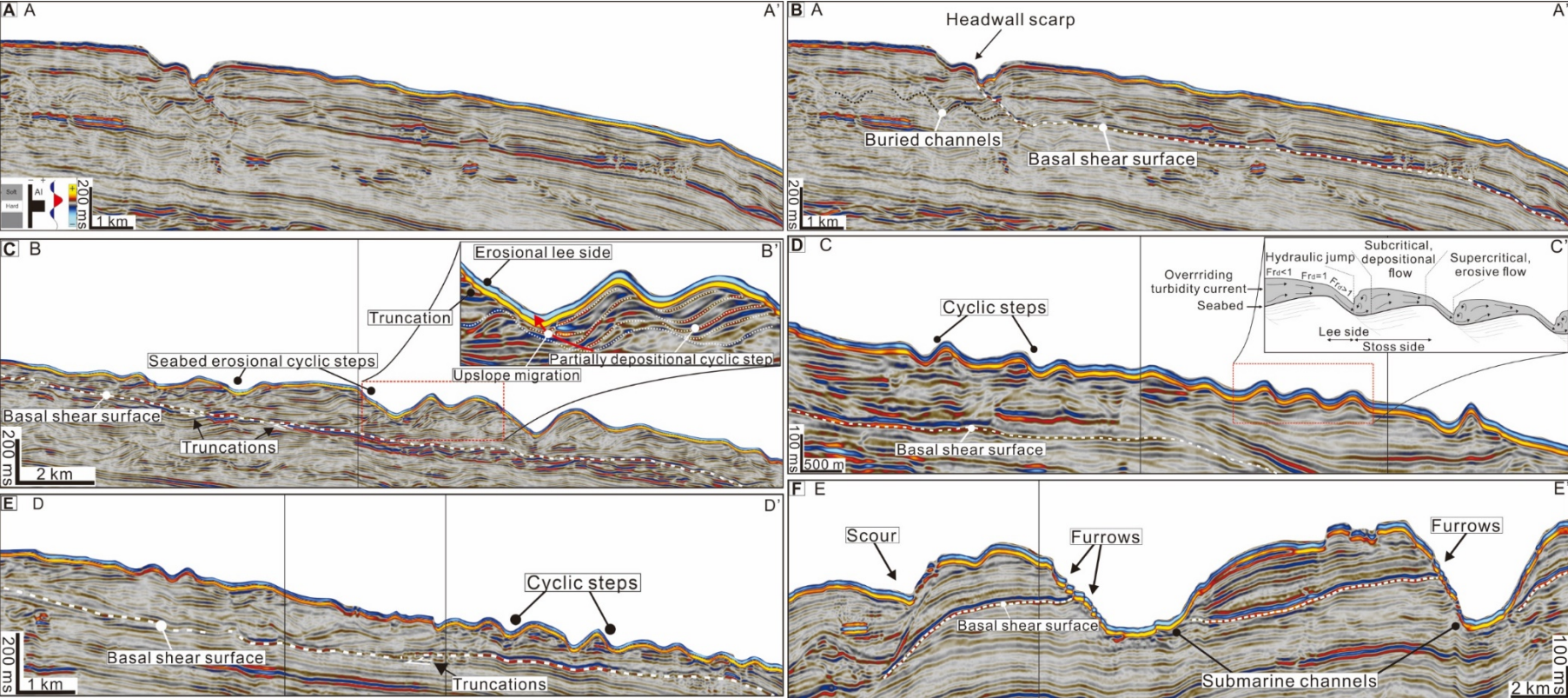


Figure 6

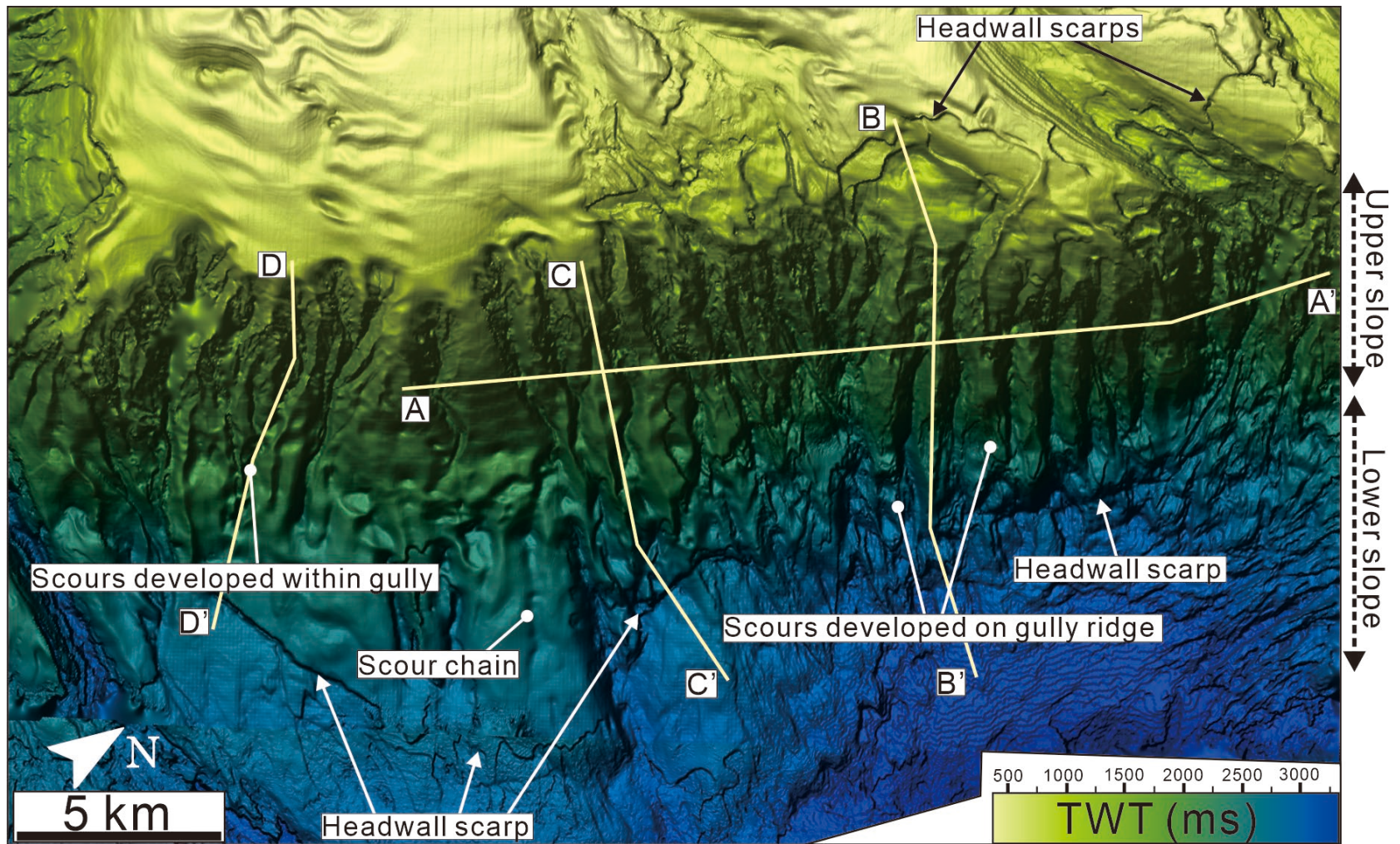


Figure 7

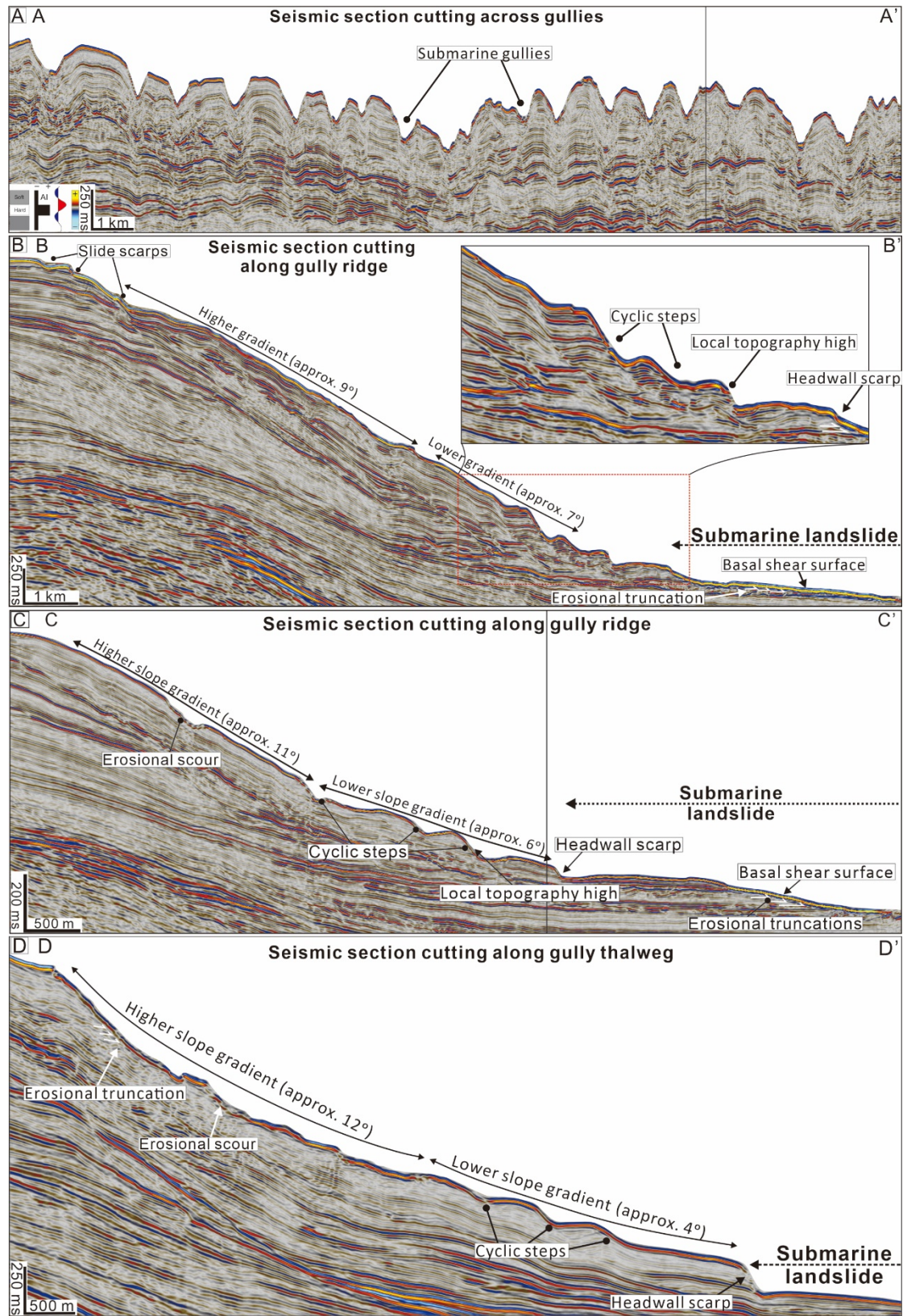


Figure 8

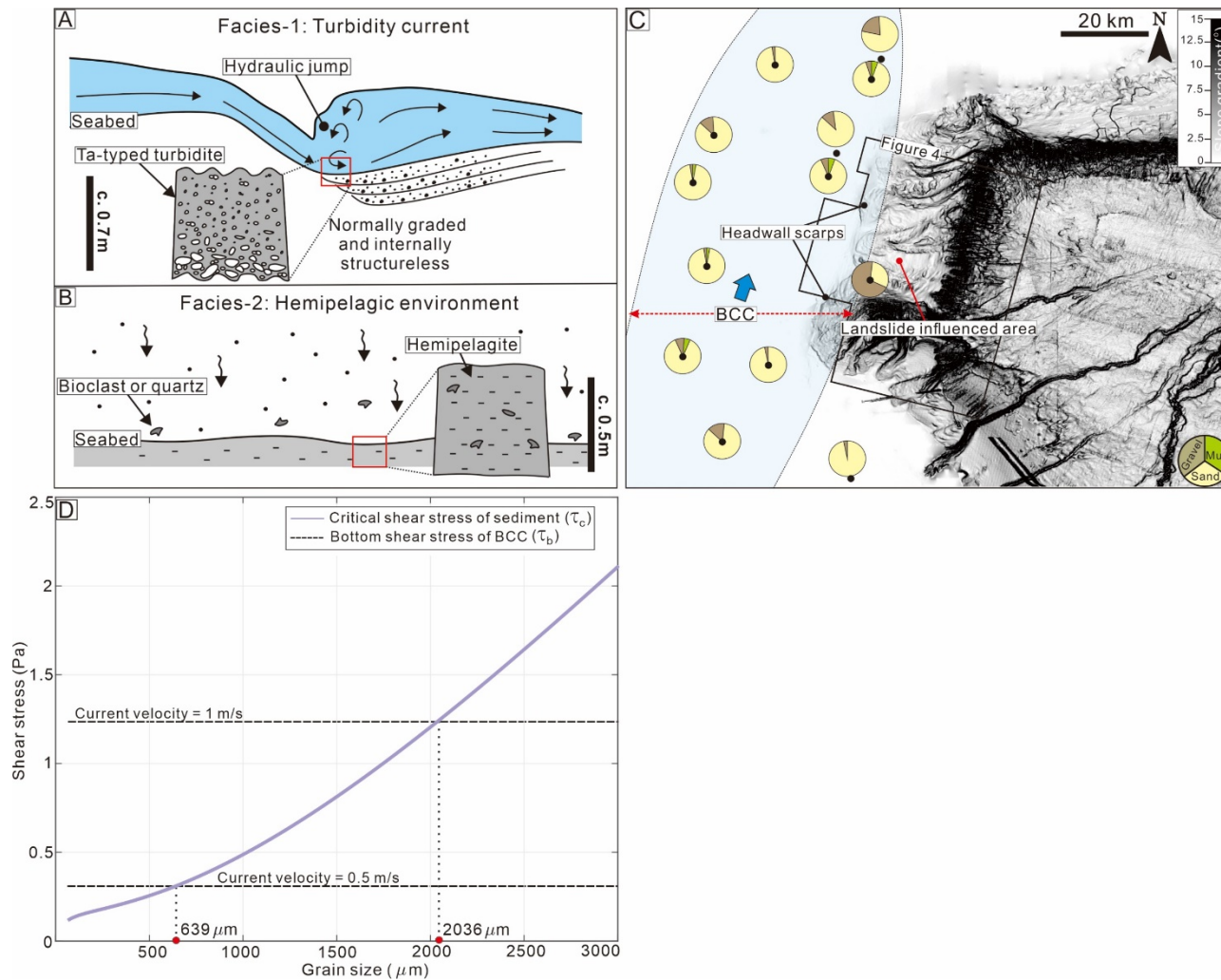




Figure 9

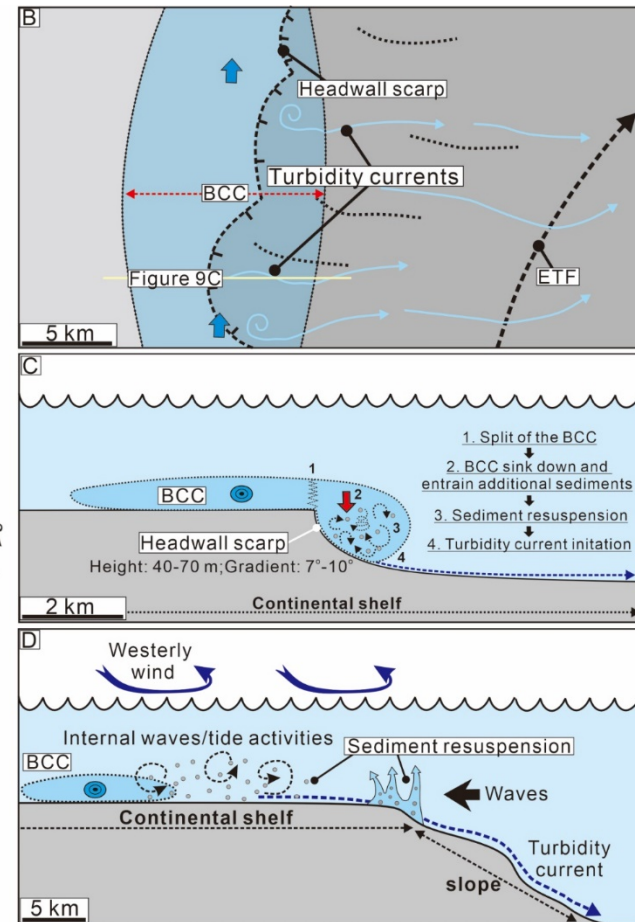
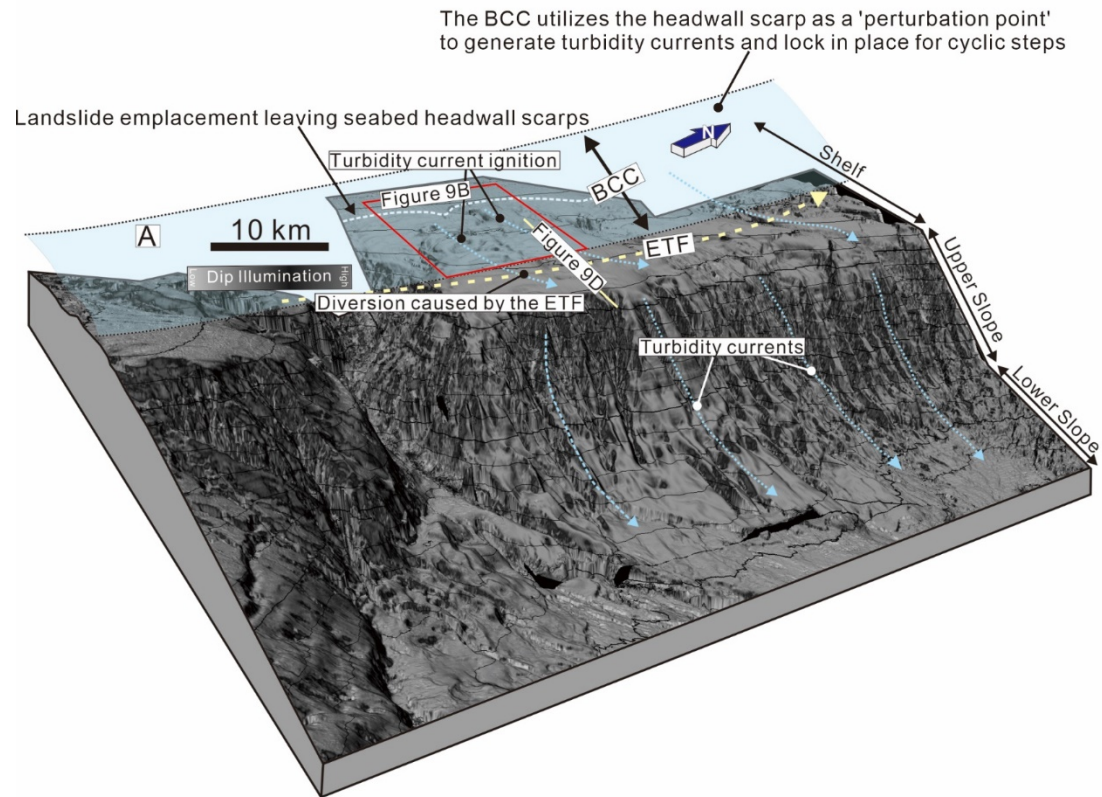


Figure 10

